PRESCRIPTION TO IMPROVE THERMOELECTRIC EFFICIENCY

A Thesis

by

SHIV AKARSH MEKA

Submitted to the Office of Graduate Studies of
Texas A&M University
in partial fulfillment of the requirements for the degree of

MASTER OF SCIENCE

May 2010

Major Subject: Materials Science and Engineering

PRESCRIPTION TO IMPROVE THERMOELECTRIC EFFICIENCY

A Thesis

by

SHIV AKARSH MEKA

Submitted to the Office of Graduate Studies of
Texas A&M University
in partial fulfillment of the requirements for the degree of

MASTER OF SCIENCE

Approved by:

Chair of Committee,	Tahir Cagin
Committee Members,	Donald Naugle
	Jun Kameoka
Chair of Materials Science and Engineering Faculty,	Tahir Cagin

May 2010

Major Subject: Materials Science and Engineering

ABSTRACT

Prescription to Improve Thermoelectric Efficiency. (May 2010)
Shiv Akarsh Meka, B.Tech, VIT University
Chair of Advisory Committee: Dr. Tahir Cagin

In this work, patterns in the behavior of different classes and types of thermoelectric materials are observed, and an alchemy that could help engineer a highly efficient thermoelectric is proposed. A method based on cross-correlation of Seebeck waveforms is also presented in order to capture physics of magnetic transition. The method is used to compute Curie temperature of $LaCoO_3$ with an accuracy of 10K. In total, over 26 systems are analyzed, and 19 presented: Chalcogenides (PbSe, PbTe, Sb_2Te_3, Ag_2Se), Skutterudites and Clathrates ($CoSb_3$, $SrFe_4Sb_{12}$, Cd $(CN)_2$, CdC, $Ba_8Ga_{16}Si_{30}$*), Perovskites ($SrTiO_3$, $BaTiO_3$, $LaCoO_3$, $CaSiO_3$, Ce_3InN*, $YCoO_3$*), Half-Heuslers (ZrNiSn, NbFeSb, LiAlSi, CoSbTi, ScPtSb*, CaMgSi*), and an assorted class of thermoelectric materials (FeSi, $FeSi_2$, ZnO, Ag QDSL*). Relaxation time is estimated from experimental conductance curve fits. A maximum upper bound of zT is evaluated for systems that have no experimental backing. In general, thermoelectric parameters (power factor, Seebeck coefficient and zT) are estimated for the aforementioned crystal structures. Strongly correlated systems are treated using LDAU and GGAU approximations. LDA/GGA/L(S)DA+U/GGA+U approach specific errors have also been highlighted. Densities of experimental results are estimated.

To my parents Dr.Shankar & Dr.Padma

and to my foster parents at A&M: Dr. Tahir and Jan

ACKNOWLEDGEMENTS

I would like to thank my advisor, Dr. Tahir Cagin for the assignment and giving me all the time in the world to solve the problem. I thank him for the support, and for injecting some of his innovative procedures, like group brainstorming, recipes to find extraordinary applications to not so extraordinary finds, etc.

I am indebted to Dr. Herschbach and all the d-scalers at A&M for continuous knowledge barters.

I would like to thank my parents for the emotional and financial support.

During my stay at A&M, I had opportunity to attend some exceptional graduate classes. Of the three classes that I enjoyed most – quantum mechanics, computational materials, and advanced material science (MSEN 602), the one that really helped me with my research was MSEN 602. Some of the homework problems happened to be starting points of my research. I thank Dr. Naugle for making the course very interesting.

Many people have inspired me and helped me improve my knowledgebase. Dr. JP Raina, (VIT University and IIT Madras) is one of them. His guidance helped me develop interest in transport physics. Conversations and email interactions with Dr. Supriyo Datta and Dr. Mark Lundstom (Purdue), and my my group members catalyzed my learning process.

I thank Dr. Kyle (Berkeley) and Dr. Cheng (Berkeley) for having innumerable late night physics discussions and crazy thought experiments.

NOMENCLATURE

Symbols

e	Electron charge
E	Energy eigenvalue
E_g	Bandgap (eV)
f_0	Equilibrium Fermi function
f_μ	Fermi-function at μ
$\hat{H}$	Hamiltonian operator
ħ	Planck's constant
k	Thermal conductivity (W/m•K)
k_e	Electrical contribution to the thermal conductivity (W/m•K)
k_l	Lattice thermal conductivity (W/m•K)
m	mass of an electron
m*	effective mass
n	Carrier concentration
pf	Power factor
S	Seebeck coefficient
T	Temperature (K)
U	Nuclear-electron interaction operator
V	External interaction potential operator
zT	Thermoelectric figure of merit
μ_m	Carrier mobility
Δ	Laplacian operator
ρ	Resistivity (Ω/cm)
σ	Electrical conductivity (S/cm)
φ	Kohn-Sham one-particle wavefunction
Ψ	Electron wavefunction

Abbreviations

2DEG	Two Dimensional Electron Gas
BTO	Barium Titanate
DFT	Density Functional Theory
DOS	Density of States
GGA	Generalized Gradient Approximation
GGA+U	Generalized Gradient Approximation with Hubbard U Correction
HF	Hartree-Fock
HH	Half-Heuslers
HS	High Spin
ICSD	International Crystal Structure Database
KH	Kohn and Hohenberg
KS	Kohn-Sham
LDA	Local Density Approximation
LS	Low Spin
L(S)DA+U	Local Spin Density Approximation with Hubbard U Correction
LSD	Least Significant Digit
MHP	Monkhorst-Pack Sampling Scheme
MO	Molecular Orbital
PAW	Projector Augmented Waves
PBE	Perdew-Burke-Ernzerhof
QDSL	Quantum Dot Superlattice
STO	Strontium Titanate
TE	Thermoelectric
VEC	Valence Electron Count
XC	Exchange and Correlation

TABLE OF CONTENTS

LIST OF FIGURES

FIGURE Page

FIGURE Page

LIST OF TABLES

CHAPTER I

INTRODUCTION

1.1 Thermoelectrics

The current demand for energy is creating social and political unrest. One way to go about the problem is to *squeeze the fruit till the last drop.* Thermoelectrics do just this! They perform the last rites by scavenging waste heat. Car exhausts, geothermal energy, home heating, industries and microchips are sources where the systems get thermally equilibrated before being put to good use. Scavenger engineering has been one of the challenges of the recent past. A plethora of materials and alloys leads to confusion on choosing an ideal material to be used as a thermoelectric. A rational approach would be to observe patterns of behavior of different classes of heat-scavengers and capture the physics to understand the rationale behind the working of these devices. Also, the quality of thermoelectric conversion has to be expressed in numbers so that one would be able to compare between two given samples and observe empirical patterns that could even help on improving the efficiency. Mathematically, the figure of merit (zT) sums it all: $zT=S^2\sigma T/k$ where S is the Seebeck coefficient which quantifies the potential change due to a temperature gradient, σ is the conductivity , T, the temperature, and k , the thermal conductivity. While S is directly proportional to the open circuit voltage ΔV developed across the structure that has just a temperature gradient ΔT ($S= \Delta V/ \Delta T$), the power factor ($pf= \frac{S^2\sigma}{\tau}$) is the closed circuit current and depends on the conductivity, σ. In order to maximize the function zT, one needs to have both Seebeck coefficient and the electrical conductivity high, and k low. But this is contradicting. How can something develop a high *emf* and even pump current? The subtlety is: the overall product is what matters. But, it is a reasonable assumption since one needs not just a voltage difference developed, but the circuit ought to be closed or there could be charge buildup finally breaking the dielectric (for very low values of σ). Beginning with

---

This thesis follows the style and format of Physical Review B.

thermocouples, thermoelectrics have a very long history. Recent trends in nanostructured materials improved efficiency 4 folds.

Doping

Type of carriers involved in the transport plays a crucial role in determining the efficiency of a thermoelectric. In general, it is advised to have higher concentration of carriers of one type. Bipolar carrier recombination adds to *k* which degrades the performance of the thermoelectric. One carrier type must dominate in order to have maximum S. Mixed conduction cancels out the net effect of charge flow as one carrier moves to the hot end and the other to the cold. Low concentration means low conductivity. Conductivity and Seebeck coefficients could be deduced from two-band models as briefed in the forthcoming section. In general, Seebeck coefficient and conductivity are given by:

$$S = \frac{8\pi^2 k_B^2}{3eh^2} m^* T \left(\frac{\pi}{3n}\right)^{\frac{2}{3}} \quad ;$$

$$\frac{1}{\rho} = \sigma = ne\mu_m$$

where m* is the effective mass, and n, the carrier concentration.

Conductivity

According to Wiedemann-Franz law: ($\kappa_e = L\sigma T = ne\mu_m LT$, Lorentz factor L=2.4 $\times 10^{-8}$ J^2 K^{-2} C^{-2}), k_e is the electronic contribution to the total thermal conductivity $k=k_e+k_l$ with the lattice thermal conductivity k_l. Charge carriers transport heat as do phonons. In Chapter II, zT is computed under the assumption that the scattering time due to electrons and phonons are equal. This crude assumption enables to find an upper bound for maximum value of zT at zero k_l. For most systems, k_l is above 75% contribution of the total *k*, and is generally unaffected by carrier concentration. Glasses are known for low k_l[a]. But, electrons in glasses are scattered very strongly making them poor thermoelectrics.

Low or high m*?

From the simple Drude model, large m* means good S but a bad σ. So, mobility is an important

[a] In glasses, the mean free path of phonons equals the inter-atomic distance, which of course, is not constant. Phonon description does no good in describing k_l. A random walk description guarantees minimal k_l. The reader is advised to read Kittel's[1] perspective on thermal conductivity in glasses.

factor in thermoelectric design. m* is directly proportional to the density of states. Flat bands (large m*) mean confined electrons with a high S. Dephasing issues and lattice thermal conductivity, scattering, and anisotropy are a summed up contribution in the overall performance. Large m* with low conductivity (for eg.:Chalcogenides) are a result of small electronegativity differences while small m* and large conductivity are a result of large electronegativity differences, but both can have a good zT.

Bottom line

One needs a "phonon-glass and an electron crystal"[2] to realize a close to ideal thermoelectric. Glass like properties are achieved by scattering phonons, engineering scattering centers and making solid-solutions. Clathrates, filled skutterudites, Quantum dot super-lattices (QDSLs), Zintl phases have so far been identified as potential candidates in the high-zT region of thermoelectric operation.

1.2 Electronic Structure and Boltzmann Transport Equation

Computationally, one could obtain reasonable electronic structures (*like the bandstructure and the density of states that are pivotal in computing transport*) by solving N electron Schrödinger equation:

$$\hat{H}\psi = \left[\hat{T} + \hat{V} + \hat{U}\right]\psi = \left[\sum_{i}^{N} -\frac{\Delta}{2} + \sum_{i}^{N} V(r) + \sum_{i<j}^{N} U(r_i, r_j)\right]\psi = E\psi$$

N being the number of electrons in the unit cell of a crystal structure, H, the Hamiltonian operator, T, the kinetic energy operator, V, the nucleus-electron interaction operator, and U, the electron-electron interaction. Such an N-electron problem deals with 3N variables requiring humongous computational power. Density Functional Theory[3] reduces the task of solving a multi-body N electron Schrödinger equation to three spatial variables of density. Density as a functional of energy was conceived separately by Thomas and Fermi. Although Thomas-Fermi[4] fails to represent the shell structure and account for the exchange interaction, it is even used today in 2DEG's[b,5], transport in graphene, etc..

[b] Currently, Thomas-Fermi (known for its simplicity) approaches are used in meso-scale condensed matter theories. Simple jelliumm models give a qualitative perspective about scattering issues, Plasmon behavior, and Friedel oscillations in 2DEGs at a economical computing cost.

DFT was put forward by two simple yet far-reaching theorems by Kohn and Hohenberg. Field perturbations and degeneracy were not taken into account in the original theorem they proposed, but eventually showed up in a refined model later on. Excited state approaches and external perturbation became add-ons in the form of time-dependent DFT.

The second KH theorem[3] states that the *exact density minimizes* the energy functional which is sum of the kinetic, Coulomb, Fock and Correlation functionals[6], while the first theorem maps the N variable problem into N "independent" equations, each of which results in a three variable density function. Density functional theory simplifies the N-particle interacting problem into non-interacting particles moving in an effective potential that includes the contribution due to Coulomb interaction. While the kinetic energy (which is a major portion of the total energy) is calculated exactly using this formalism, exchange and correlation has been a problem for the past 3 decades of its inception. There are hundreds of papers dealing with the proper functional form of the exchange and correlation. Hartree-Fock[6] for example, naturally treats exchange and it is for this reason that DFT uses a very similar Fock (Slater) like term. The initial functional (LDA[7]$(Exchange - Correlation\ functional) E_{xc} = \int d^3r\ \epsilon_{xc}(n_\downarrow, n_\uparrow) n(r)$ assumed a uniform electron gas (advanced Thomas-Fermi model). The correlation functional in the LDA regime looks like: $\varepsilon_c = Aln(r_s) + B + r_s(Cln(r_s) + D)$, A,B,C,D are parameterized constants, and rs is the Wigner-Sietz[7] radius. And even the advanced GGA[7] approach employs a similar functional term except that it has derivatives of the density (applicable where density changes abruptly like in metals).

The DFT Procedure

Any observable (*like* energy, momentum, etc.) O could be written as:

$$O[n_0] = \langle \psi[n_0] | \hat{O} | \psi[n_0] \rangle$$

and the ground state energy which is a *functional* of exact density n_0 is given as :

$$E_0 = E[n_0] = \langle \psi[n_0] | \hat{T} + \hat{V} + \hat{U} | \psi[n_0] \rangle$$

The external potential $\langle \psi | \hat{V} | \psi \rangle$ is written as: (here is where one lumps the correlation into some functional form)

$$V[n_0] = \int V(r) n_o\,(r) d^3r$$

T[n] and U[n] are independent of the type of nucleus (atomic number) and hence are called universal functionals. And it is now enough to minimize the functional:

$$E[n] = T[n] + U[n] + \int V(r) n_o\,(r) d^3 r]$$

Initially, one solves the energy functional without an *explicit* e-e term for each shell s:

$$E_s[n_0] = \langle \psi_s[n] | \hat{T}_s + \hat{V}_s | \psi_s[n] \rangle$$

where $\hat{V}_s = \hat{V} + \hat{U} + (\hat{T} - \hat{T}_s)$ and T_s is the kinetic energy operator of the shell s, and the optimization rules that include the xc effects, help minimize the kinetic energy. One then solves *s*-shell single particle non-interacting system (Kohn-Sham Hamiltonian): (in atomic units)

$$[-\Delta + V_s(r)]\phi_i(r) = \varepsilon_i \phi_i(r)$$

where the density and V_s are given by:

$$n(r) = n_s(r) = \sum_i^N |\phi_i(r)|^2$$

$$V_s(r) = V(r) + \int \frac{n_s(r')}{|r-r'|} d^3 r' + V_{xc}[n_s(r)].$$

The trick used to compute guess density is to superpose the already parameterized atom-dependent basis sets. A linear combination of these basis functions produce molecular orbitals (MO coefficients) or energy bands. The optimization Hessian has values corresponding to the mixing rules. V_s obtained, is supplied as input to the KS Hamiltonian. This process reiterates until the convergence (difference of successive ε's < tolerance) is reached.

Boltzmann Transport[8]

As with the continuity equation, the value [*Av(x)g(x)dt-Av(x+dx)g(x+dx)dt*]- represents the number of particles between *g(x+dx) and g(x)* [with g being the density] flowing perpendicular to the plane of area A with velocity *v(x)* at *g(x)* and *v(x+dx) at g(x+dx)*. And hence,

$\frac{dg}{dt} = \frac{-d}{dx}(v(x)g(x,t))$.

To the above equation, Boltzmann added a viscous term that includes the effect of scattering and hence $\frac{dg}{dt} = \frac{-d}{dx}\big(v(x)g(x,t)\big) + \frac{dg}{dt}\Big]_{coll}$

In the Hamilton notation[c], the group velocity of an electron is given as:

$$v(i,k) = \nabla_k \varepsilon_{i,k}.$$

[c] Dirac's prelude[9] to quantum mechanics is an excellent description of the connection with Hamilton formulation.

The conductivity could be defined as: $\sum(v^2)$ DOS(E) or more precisely:

$$\bar{\sigma}_{\alpha\beta}(\varepsilon) = \frac{1}{N}\sum_{i,k} \tau \cdot \nu_\alpha(i,k) \cdot \nu_\beta(i,k) \cdot \frac{\delta(\varepsilon-\varepsilon_{i,k})}{d\varepsilon} \qquad (1)$$

and Seebeck coefficient is given by :

$$S_{\alpha,\beta}(T,\mu) = \frac{1}{T\Omega\bar{\sigma}_{\alpha\beta}(T,\mu)} \int \bar{\sigma}_{\alpha\beta}(\varepsilon)\,(\varepsilon-\mu)\left[-\frac{\partial f_0(T,\varepsilon,\mu)}{\partial\varepsilon}\right] d\varepsilon \qquad (2)$$

where μ is the electrochemical potential, f_o is the Fermi function, $\varepsilon_{i,k}$, the energy of i^{th} band and k^{th} k-space sample, Ω the volume of the unit-cell and $\frac{\partial f_0}{\partial\varepsilon}$ is the thermal broadening function which smears the discrete energy levels.

1.3 Two-Band Models

Equations (1) and (2) are used to compute S vs T curves (Fig.1.1) for different configurations (Table.1.1).

TABLE 1.1. Possible permutations of varying magnitudes of m_{cb} and m_{vb}. Types of possible configurations m_{cb} and m_{vb} are effective masses of conduction band and valence band. The figure *fig.1.1* summarizes the behavior of various combinations of effective masses, position of the Fermi energy and bandgaps to determine the behavior of Seebeck coefficient. Most of the systems in the forthcoming chapters could be explained by these simple two band models.

Type	Description
A	Small bandgap and Fermi positioned symmetrically, small m*
B	Large bandgap and Fermi positioned symmetrically, large m*
C	Large bandgap and Fermi positioned symmetrically, small m*
D	Small bandgap and Fermi positioned symmetrically, $m_{cb} > m_{vb}$
E	Large bandgap, and Fermi positioned symmetrically, $m_{vb} > m_{cb}$
F	Small bandgap, and Fermi positioned symmetrically, $m_{vb} > m_{cb}$
G	Large bandgap, and Fermi positioned symmetrically, $m_{vb} < m_{cb}$
H	Large bandgap, and Fermi positioned asymmetrically, $m_{vb} < m_{cb}$

TABLE 1.1 Continued.

Type	Description
I	High bandgap, and Fermi positioned symmetrically, $m_{vb} = m_{cb}$
J	Small bandgap, and Fermi positioned asymmetrically, $m_{vb} = m_{cb}$

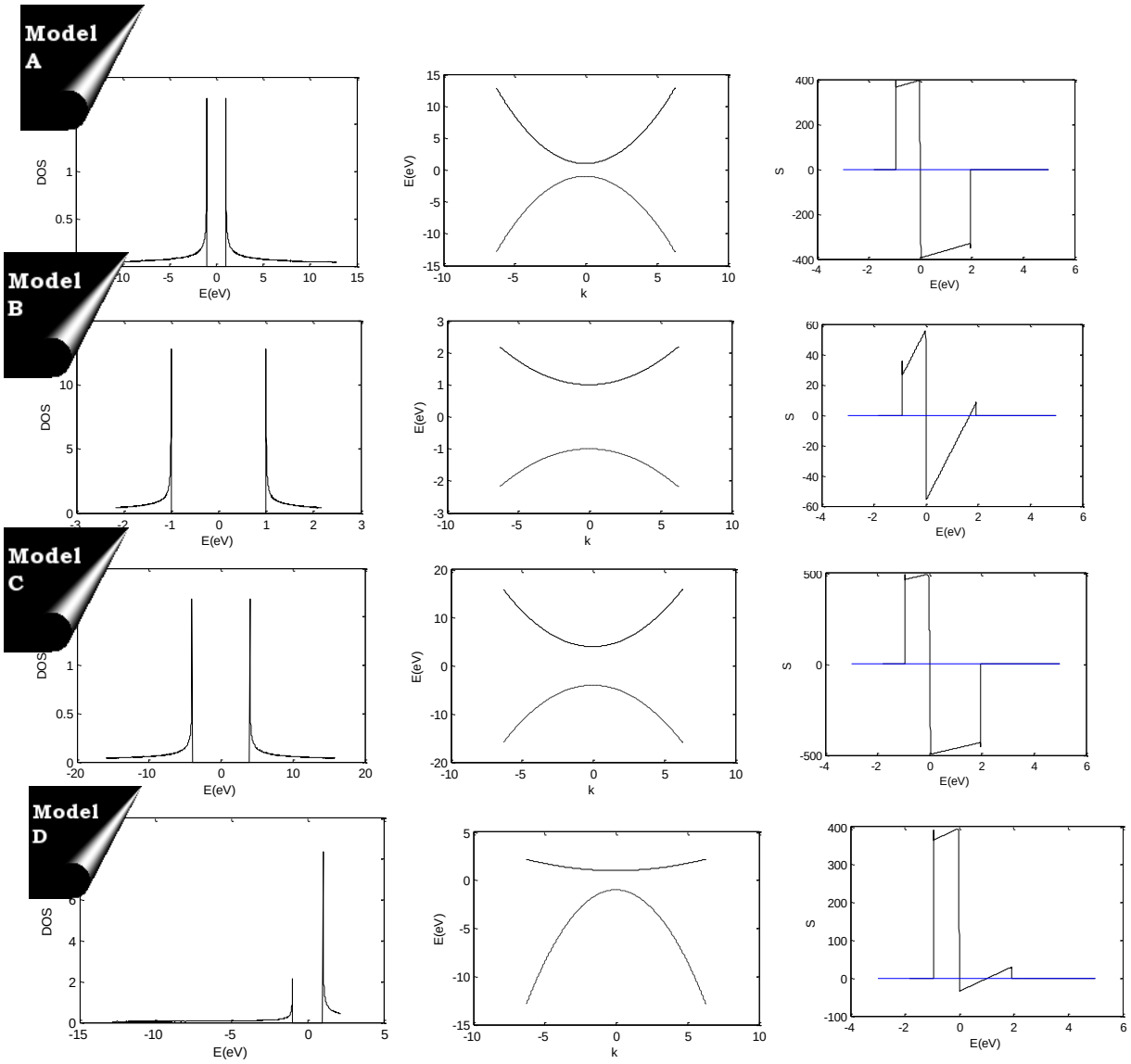

FIG. 1.1. TE Two-band models. Density of states (DOS (ε-μ)), band-structure and Seebeck coefficient S(ε-μ) plots of crystal structures with a) *narrow bandgap small m** b) *narrow bandgap large m** c) *large bandgap, small m** d) *narrow bandgap, small* m_{vb} *large* m_{cb} .

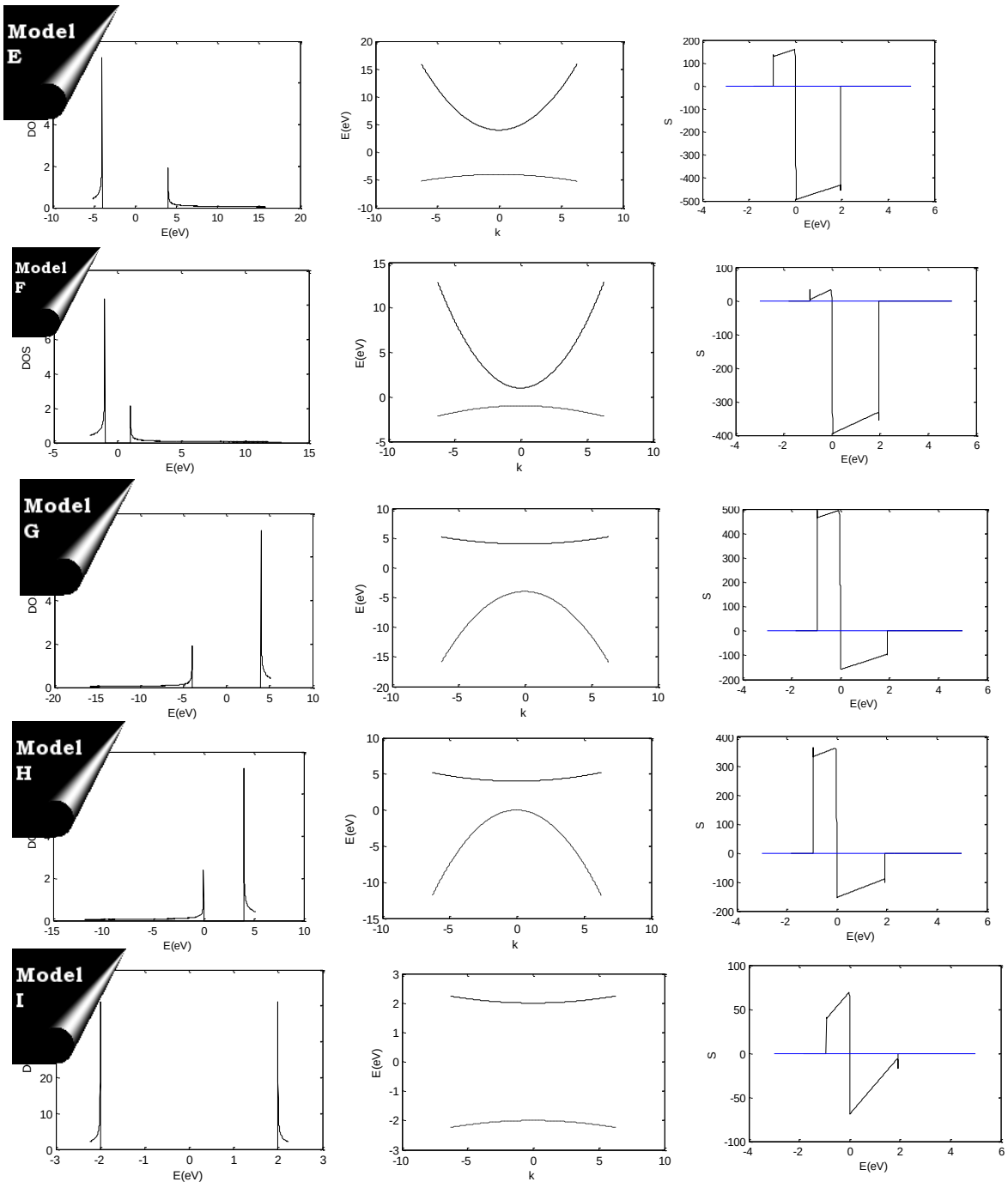

FIG. 1.1 Continued. e) *large bandgap , small mvb, large mcb* f) *Fermi positioned at zero for narrow bandgap, large* m_{vb} *small* m_{cb} *results in* S(-) g) *Fermi brought close to VB results in decrease of* S(+) h) *Fermi positioned at VB results in large S(+) for large* m_{cb} *and small* m_{vb} i) *Fermi at zero in the wide bandgap crystal with both* m_{vb} *and* m_{cb} *high..*

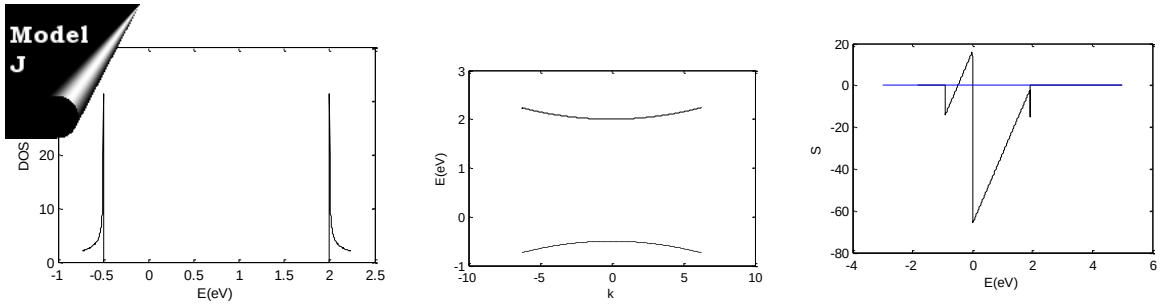

FIG. 1.1 Continued. j) *moderate gap and Fermi position asymmetrically with both large m_{cb} and m_{vb}.*

CHAPTER II

THERMOELECTRICITY IN CRYSTAL STRUCTURES

2.1 Chalcogenides

A binary compound with one element derived from the group XVI is classified as a Chalcogenide. There are exceptions, however, for example, oxides. But, in general, Selenides and Tellurides are tagged by this name. The Chalcogenide samples under this study (Fig. 2.1) include: Lead Chalcogenides – PbSe (Fig. 2.2) and PbTe (Fig.2.3-2.10), β-Ag_2Se (Fig. 2.11-2.14) , and Sb_2Te_3 (Fig.2.5). Lead Chalcogenides have a Rocksalt (NaCl) structure and the lattice symmetry (Fm3m) enables spot-on DFT calculations requiring just two atoms in the primitive cell. It is also surprising that simple structures such as these have a moderate thermal conductivity[10]. β-Ag_2Se is orthorhombic (below 160 K) while Sb_2Te_3 is trigonal. Of the four compounds that were analyzed for various doping concentrations, the Lead Chalcogenides showed good thermoelectric behavior at higher temperatures (~600K in agreement with experimental values[11]) while Sb_2Te_3 is efficient at room temperatures. β-Ag_2Se happened to be a "bad-insulator" with low Seebeck coefficients. Experimental Seebeck coefficients were fit to obtain doping concentrations, relaxation times of PbSe, PbTe and β-Ag_2Se .

Lead Chalcogenides (PbSe and PbTe)

Lead Chalcogenides have recently gained a lot of attention for their moderate thermal conductivity. Poudeu *et. al*[12] proposed $Pb_{9.6}Sb_{0.2}Te_{10-x}Se_x$ compounds with a zT of 1.2 at 650 K. Bandstructure of PbTe[13] and the positioning of Fermi level (Fig.2.2.a) resemble two-band model ***a***: the effective masses (m_{vb},m_{cb}) being almost the same, and hence we predict some kind of symmetry[14] and high zT (Fig. 2.2). The bandgap was observed to be 0.28 eV [exp.: 0.28] for PbSe, and 0.3 [exp:. 0.35] for PbTe. Deviation in lattice parameters of PbSe and PbTe amount to 1% and 1.5%. PBE functional was used for both exchange and correlation (xc). The SvsT fits estimate the doping concentration to be around 13.2E18 /cm^3 for PbSe (Fig. 2.2) and 3.11E19 /cm^3 in PbTe (Fig. 2.4). In the case of PbSe, the experimental values do not make a perfect fit to theory.

Model A

Lead Selenide (PbSe)

Experimental

Structure: cubic (NaCl)

[a b c]: 6.14

Bandgap[16]: 0.28 eV

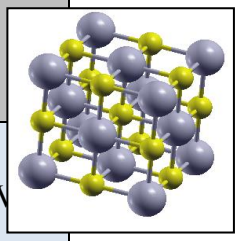

DFT (PBE)

Energy Cutoff: 300 eV

[a b c]: 6.21

Bandgap: 0.35 eV

K-Points: 8000

Maximum zT: 0.9 at 200K

Atoms: 2

Model A

Lead Telluride (PbTe)

Experimental

Structure:cubic (NaCl)

[a b c]: 6.46

Bandgap[15]: 0.3 eV

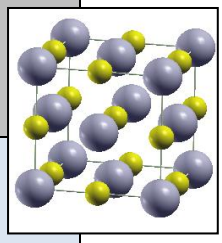

DFT (PBE)

Energy Cutoff: 300 eV

[a b c]: 6.56

Bandgap: 0.27 eV

K-Points: 21952

Maximum zT: 0.98 at 750K

Atoms: 8

Model F

Antimony Telluride (Sb_2Te_3)

Experimental

Structure: trigonal

[a b c]: 4.25 4.25 29.96

Bandgap[17]: 0.28 eV

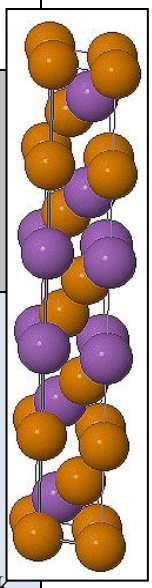

DFT(PBE)

Energy Cutoff: 300 eV

[a b c]: 4.34 4.34 31.20

Bandgap: 0.33 eV

K-Points: 15625

Maximum zT: 0.8 at 200K

Atoms: 5

Model A

Silver Selenide (Ag_2Se)

Experimental

Structure: orthorhombic

[a b c]: 4.34 7.06 7.767

Bandgap[14]: 0.12

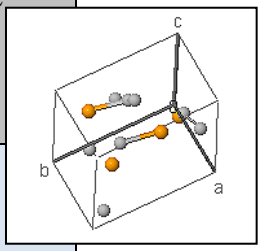

DFT(PBE)

Energy Cutoff: 400 eV

[a b c]: 4.53 7.13 7.7

Bandgap: 0.07 eV

K-Points: 1728

Maximum zT: -90 at 100K

Atoms: 12

FIG. 2.1. Summary of lattice parameters, computational specifications, and band gaps in Chalcogenides.

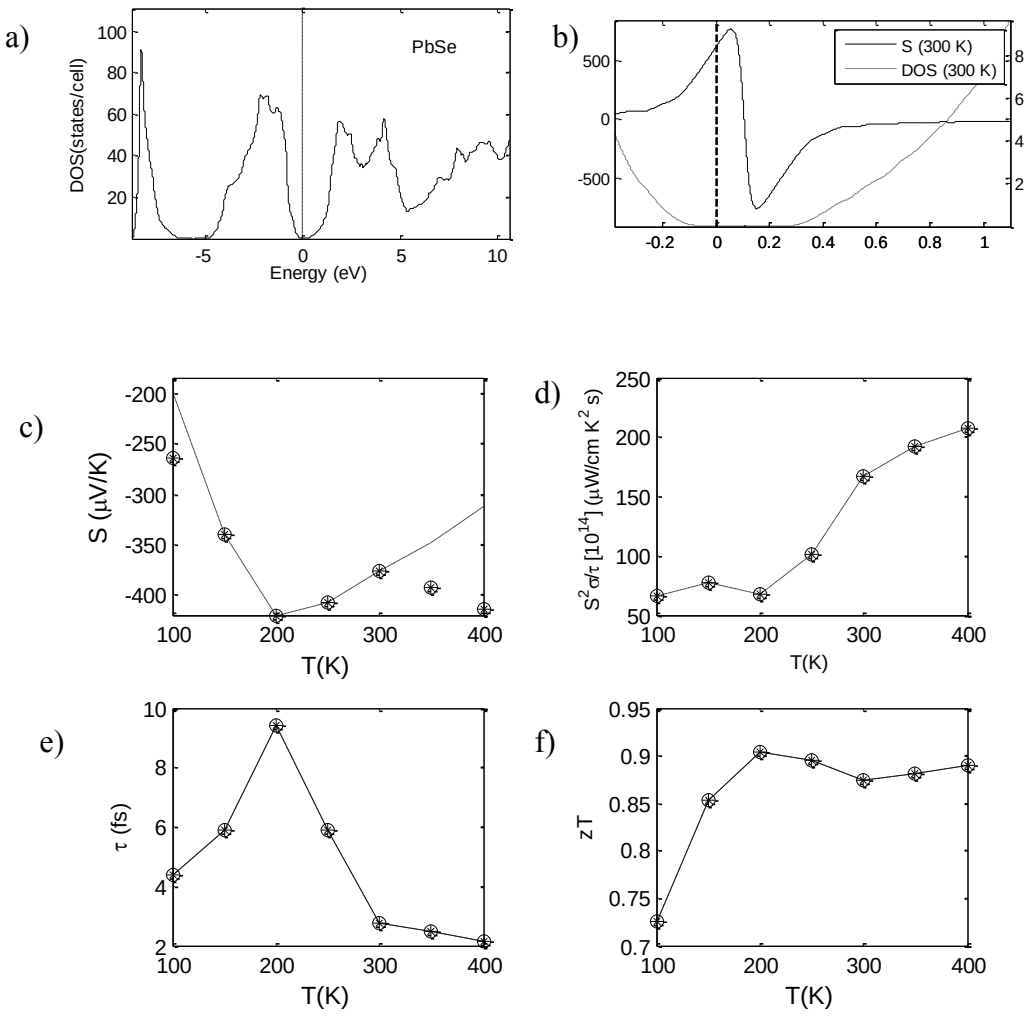

FIG. 2.2. TE performance metrics of PbSe. a) DOS of Lead selenide calculated using PBE functional. The bandgap of 0.28 eV is observed which coincides with experimental value of 0.28 eV [16]. b) Figure is a close-up view of the previous plot with Seebeck coefficient (in μV/K) on the left vertical axis and DOS on the right. c) Calculated values are plotted alongside experimental results. The calculations closely follow experimental results for cases where the bin size is too tight ($\Delta\sim10^{-5}$), and also for $\Delta\sim10^{-4}$. The mean averaged errors are 0.19 for the coarsely defined value of 10^{-4} and -6.52 for a finer tolerance. d) Estimated power factor values are compared to the experiment. The error that carries on from S-T curve, is more than doubled as shown in the plot (the deviation being 67 μV/K). The additional overhead comes from the erroneous σ/τ term. e) Experimentally observed conductance is compared to the calculated σ/τ to extract τ. f) Upper bound of zT. Lattice thermal conductivity is not taken into account in the calculation.

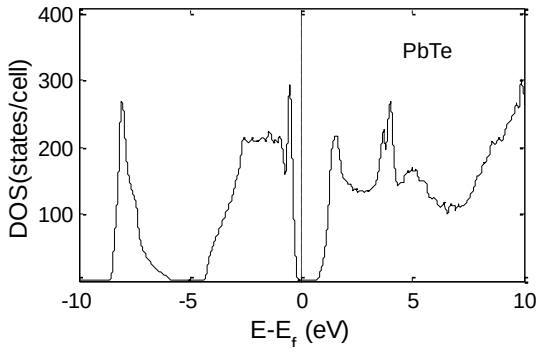

FIG. 2.3. DOS plot of PbTe. PBE functional is used to calculate the electronic structure (above). The estimated bandgap is close to 0.35 eV as compared to the experimental[15] 0.3 eV.

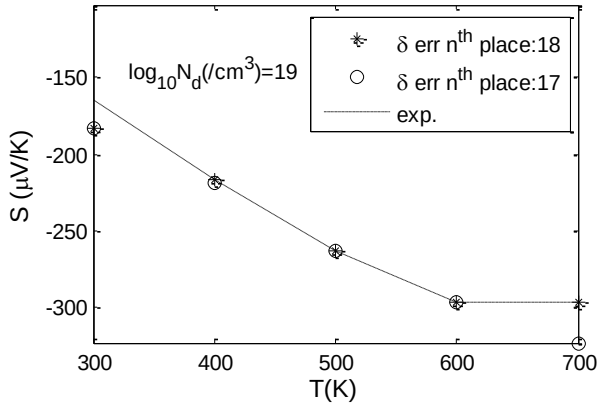

FIG. 2.4. Experimental PbTe S vs T fit. As with the selenide version, the S-T curves in PbTe are also insensitive to a considerable change in the levels of tolerance. The doping concentration is estimated to be around: 1.38E019.

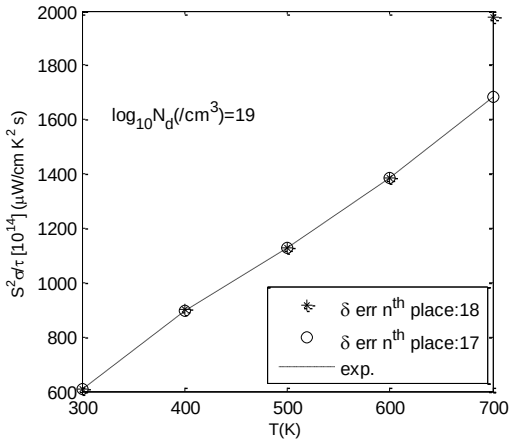

FIG. 2.5. Power factor plot of PbTe. Plot shows that both the coarse and fine tolerance series values again follow the experimental result.

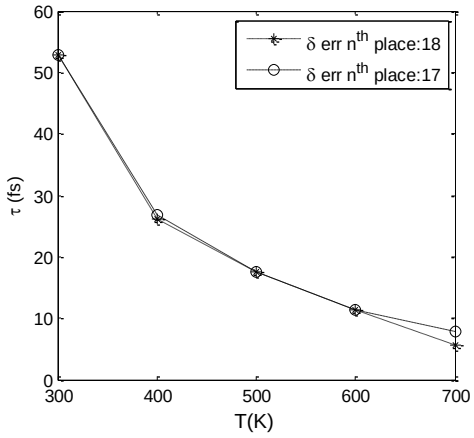

FIG. 2.6. Relaxation rates in PbTe. T Relaxation rates extracted from experimental conductance values.

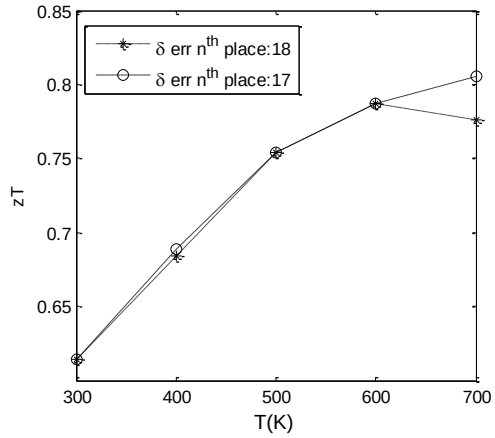

FIG. 2.7. PbTe zT plot. $k_{l\text{-}th}$ is assumed to be zero. Hence, from now on, any mention of zT is the maximum practical one can have (ref. Chapter I-alloying) without changing the electronic structure.

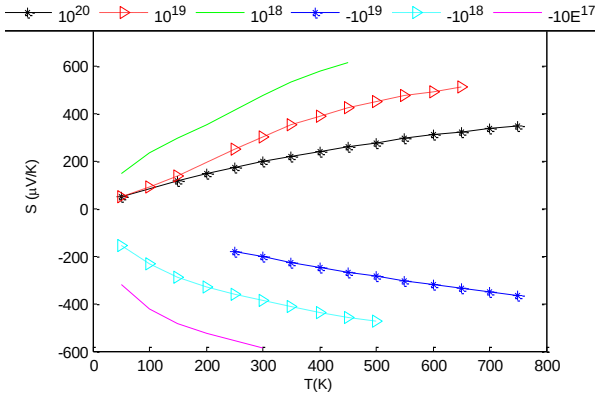

FIG. 2.8. PbTe S-T curves for various doping concentrations. A negative value in the doping concentration implies n-type dopant.

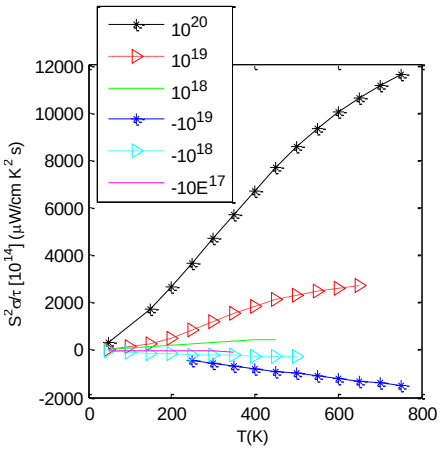

FIG. 2.9. PbTe pf -T plot for different doping levels. The power factor on the doped n-side has a lower slope owing to the distance of the conduction band edge from the Fermi level.

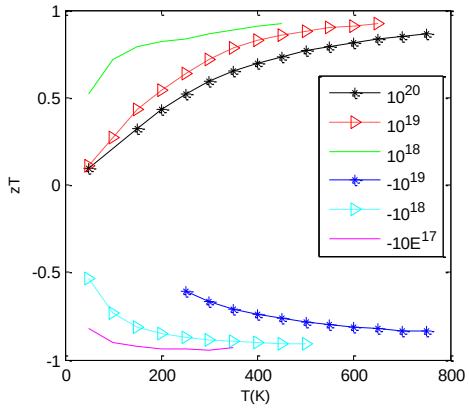

FIG. 2.10. PbTe zT-T plot for different doping concentrations. Performance is better at lower doping levels.

The rationale is as follows: the very crude assumption of bandgap independence on temperature fails in this case[a]. Decrease in bandgap proves more costly (in transport) than increasing it by the same amount (as it is apparent from the simple models presented in the earlier chapter). PbSe is very sensitive to temperature dependence on bandgap[14].

[a] Rigid band model was assumed for all BTE calculations

A zeroth order estimate: large atomic ratio differences lead to higher amplitude of phonon scattering[b,18] (Mass %Δ – PbSe: 0.37, PbTe: 0.67) which implies the bandgap is robust to temperature changes in PbTe.

β-Ag_2Se

β-Ag_2Se is known for its low lattice thermal conductivity (~5mW cm^{-1} K), low resistance (5E(-4) ohm cm^{-1}) and a reasonably good Seebeck coefficient[19] (150 μV/K). Bandgap of Ag_2Se was estimated to be 70 meV (Fig. 2.11) as compared to the experimental value[14,20] of 120 meV. Narrow-band semiconductors (Ag_2Se, Half-heusler) often are victims of the infirmities of DFT. Narrow-band gaps are underestimated as well! The degree of error is critical in determining Seebeck coefficients (Fig.2.12). Wide bandgap semiconductors show minimal deviation (as apparent from the two-band models (a and c)) for the percentage change in the Seebeck coefficient is mild. Further, relaxation time and zT values are extracted from the experimental fit (Fig. 2.13-2.14).

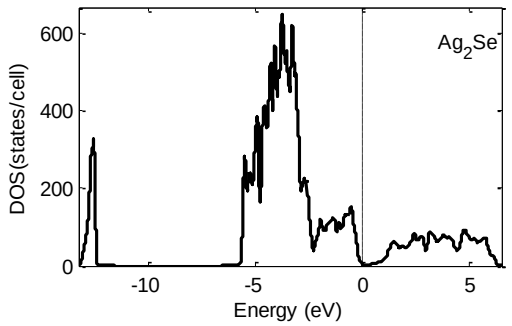

FIG. 2.11. DOS plot of Ag_2Se crystal. The electronic states are minimal but exist right at the Fermi level making Ag_2Se a "bad"-insulator.

[b] Disorder scattering is prominent in elements that have large atomic mass differences. Short wavelength phonons are scattered and hence several modes are "annihilated". Non-availability of phonon modes reduces e-ph scattering.

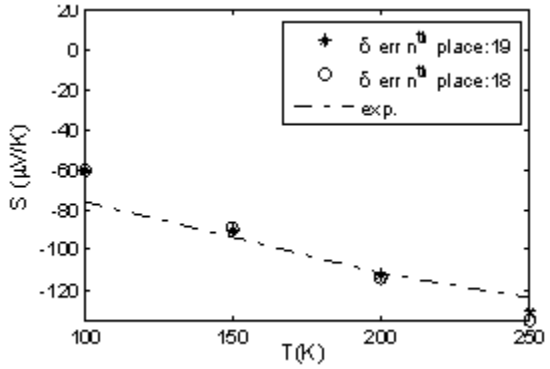

FIG. 2.12. Experimental Ag_2Se S-T fits. The doping concentration is estimated to be around 18.6E19.

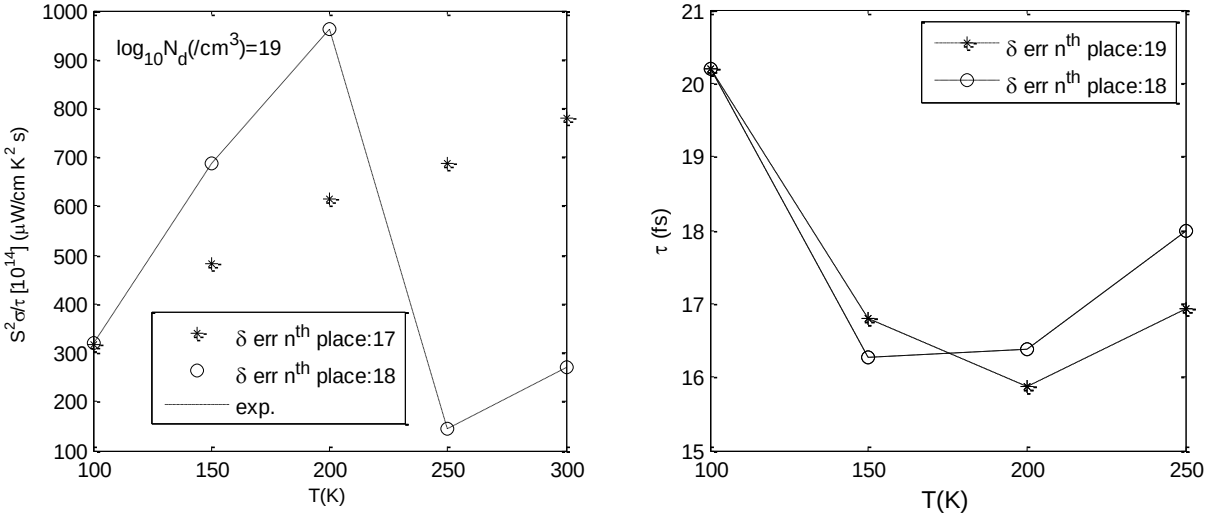

FIG. 2.13. Ag_2Se pf-T and relaxation time plots. The results obtained from transport calculations are fit to experiment. Discrepancies in the fit are a result of phase change at 160K. Misfit of data is a diagnostic of a wrong calculation, observation of which is used as a tool to estimate the Curie temperature in Chapter III.

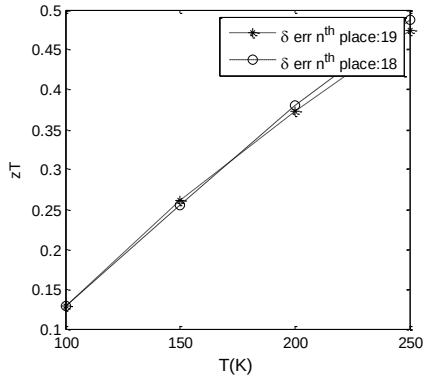

FIG. 2.14. zT vs T plot for β-Ag_2Se crystal.

Computational details: Generalized Gradient Approximation (GGA) is used for exchange and correlation. A maximum error of 4% (see page 50) . 12^3 (1728) Monkhorst-Pack[21] (MHP) sampling points (in the reciprocal grid) are used. The carrier concentration was found to be 1.86E20. The results of experimental fit of the Seebeck coefficients to extract the Scattering time are presented in *fig.2.12*. Scattering time (τ) vs T misfit is attributed to the change of phase of Ag_2Se. Ag_2Se changes phase from orthorhombic-β to cubic-α[22] at 160^o C

Sb_2Te_3

Bi_2Te_3-Sb_2Te_3 solid-solutions have a high thermoelectric efficiency[23]. Anisotropy results in phonon and impurity scattering thereby decreasing the lattice thermal conductivity. Electronic structure calculations of such super cells is dealt with by Wang and Cagin[24]. Single Sb_2Te_3 cells also show good thermoelectric behavior as shown in the figure (Fig.2.15). Again, as conjectured earlier (in Chapter I), the symmetrical location of the Fermi level enables n or p type dopants of a fixed doping concentration to return similar magnitudes of thermoelectric parameters. As it is apparent from zT vs T plot, doping the concentration helps tune max{zT} to give optimal performance at a particular temperature.

Computational details: A maximum deviation of about 4% is observed in the lattice parameters. PBE functional is used for exchange and correlation. 25^3 (15625) point MHP k-space grid is used. The band gap computed was 0.28eV as compared to the experimental value of 0.33eV. Sb_2Te_3 has a trigonal structure (Pearson number: 166).

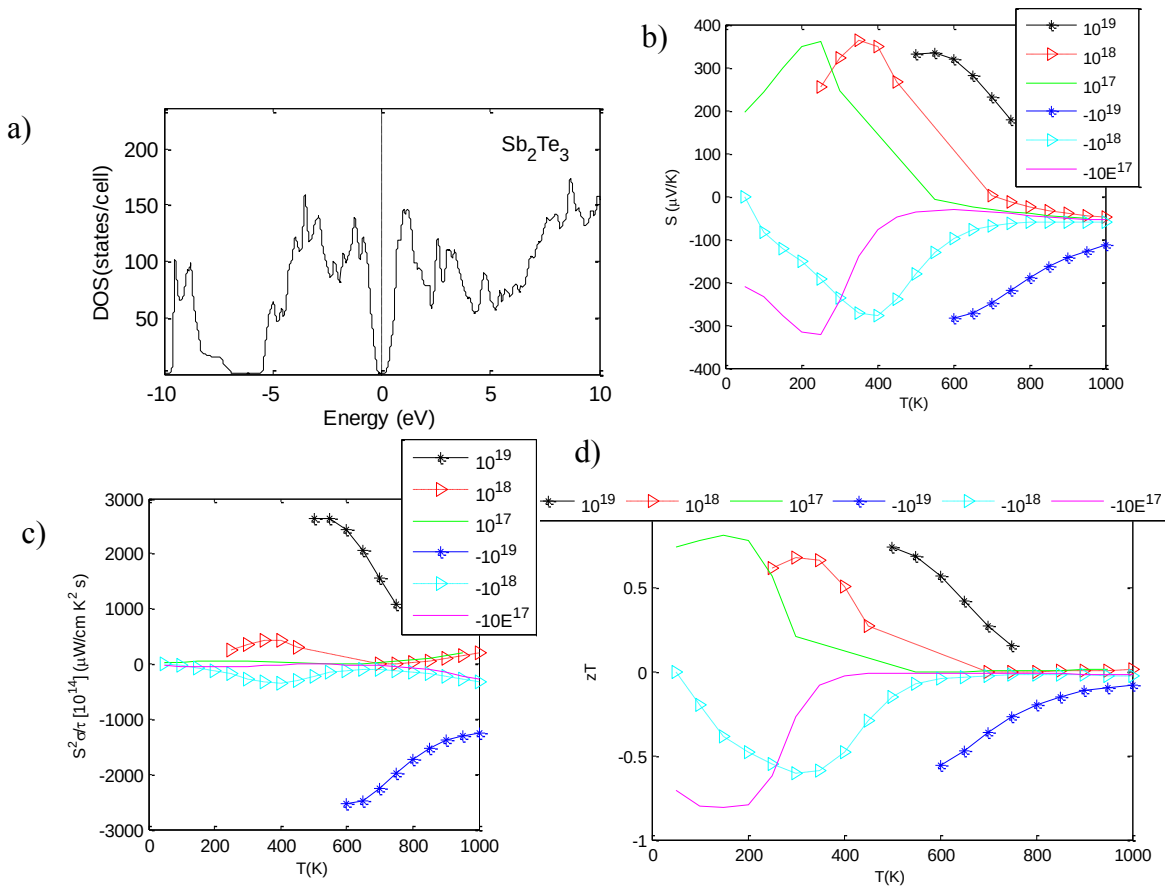

FIG. 2.15. TE performance metrics of Sb_2Te_3. a)DOS plot, b) Seebeck coefficient c) power factor d) zT of Sb_2Te_3.

2.2 Half-Heuslers

Half-heuslers(HH) are Heusler structures with half atoms missing (Fig.2.16). Valence electron count (VEC) determines the electronic structure of Heusler[25] and HH structures[26]. VEC count

Model A

ZrNiSn

Experimental

Structure: cubic

[a b c]: 6.11

Bandgap: 0.12[27]

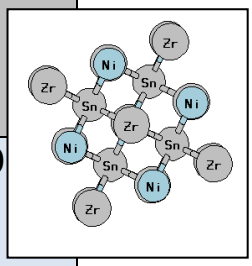

DFT (L(S)DA+U)

Energy Cutoff: 450

[a b c]: 6.2

Bandgap: 0.18 eV

K-Points: 17576

Maximum zT: 0.7 around 200K

Atoms: 2

Model H

Niobium Ferrous Antimonide(NbFeSb)

Experimental

Structure:cubic

[a b c]: 5.96

Bandgap:(-)

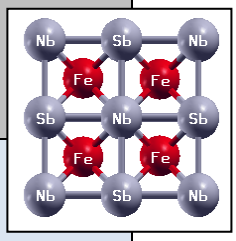

DFT(LDA)

Energy Cutoff:400

[a b c]: 5.96

Bandgap: 0.075 eV

K-Points: 5832

Maximum zT: 1.14 below 400K

Atoms: 3

Model H

CoSbTi

Experimental

Structure: cubic

[a b c]: 5.88

Bandgap: 0.95[28]

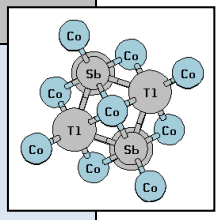

DFT(PBE)

Energy Cutoff: 450

[a b c]: 5.89

Bandgap: 0.98 eV

K-Points: 13824

Maximum zT: 0.8 at over 1000K

Atoms: 12

Model A

Lanthanum Aluminium Silicide (LaAlSi)

Experimental

Structure: cubic

[a b c]: 5.94

Bandgap: (-)

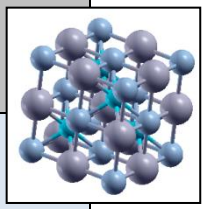

DFT(GGA)

Energy Cutoff:450

[a bc]: 5.94

Bandgap: 0.39 eV

K-Points: 8000

Maximum zT: 0.8-0.7 around 200K

Atoms: 3

FIG. 2.16. Summary of lattice parameters, computational parameters, and band gaps in Half-Heuslers.

of 18 implies existence of bandgap in HH[29]. HH are usually narrow bandgap semiconductors[c] that have moderate zT at high temperatures[30]. The important contributing factor to this "moderateness" is the thermal-conductivity (for eg. NiSnZr has *k* close to 10 W/m·K). But, their thermal conductivities are obviously lower than their Heusler counterparts. Tailoring the crystal could improve the thermal conductivity. For eg. in NiSnZr, Zr is replaced by a heavier Hf[31] and the thermoelectric conductivity was halved. The maximum zT in NiSnZr was found to be 0.7 which also happens to be an experimental prediction[31]. Most HH are n-type. It is still a challenge to find their intrinsic p-type and Si-Ge like alter ego. Asymmetry in the position of the Fermi level in the case of LaAlSi and CoSbTi implies they are a natural p-type alloys. In this study, four HH alloys were studied: i) CoSbTi (Fig.2.17) ii) NiSnZr (Fig. 2.18-2.20) iii) LaAlSi (Fig. 2.21) and iv)NbFeSb (Fig.2.22-2.24).

An ideal thermoelectric not only has a high zT, but work efficiently for a broad temperature range. While three of the four observed structures performed well at 200 K (with zT ~ 0.75), counter intuitive to the generalized perception of zT in HH, NbFeSb has a high zT and behaves as a good thermoelectric over a wide temperature range and for a given doping concentration.

CoSbTi

From the functional form of the Seebeck coefficient, it is apparent that sharp DOS would lead to high S. These ternary inter-metallic structures resemble the MgAgAs cubic types. The transport coefficients of CoSbTi are fit to experiments (Fig.2.17). The doping concentration is estimated as 1.03E20 /cm^3. The bandgap was found to be : 0.98 eV (exp.:0.95). PBE functional was used for both exchange and correlation. The lattice parameters are almost the same as the experiment (deviation of 0.002%).

[c] Take the case of NiSnZr, the bandgap is thanks to the hybridization of the d-shell electrons of Ni and p-electrons of Sn , and also contribution due to exchange splitting.

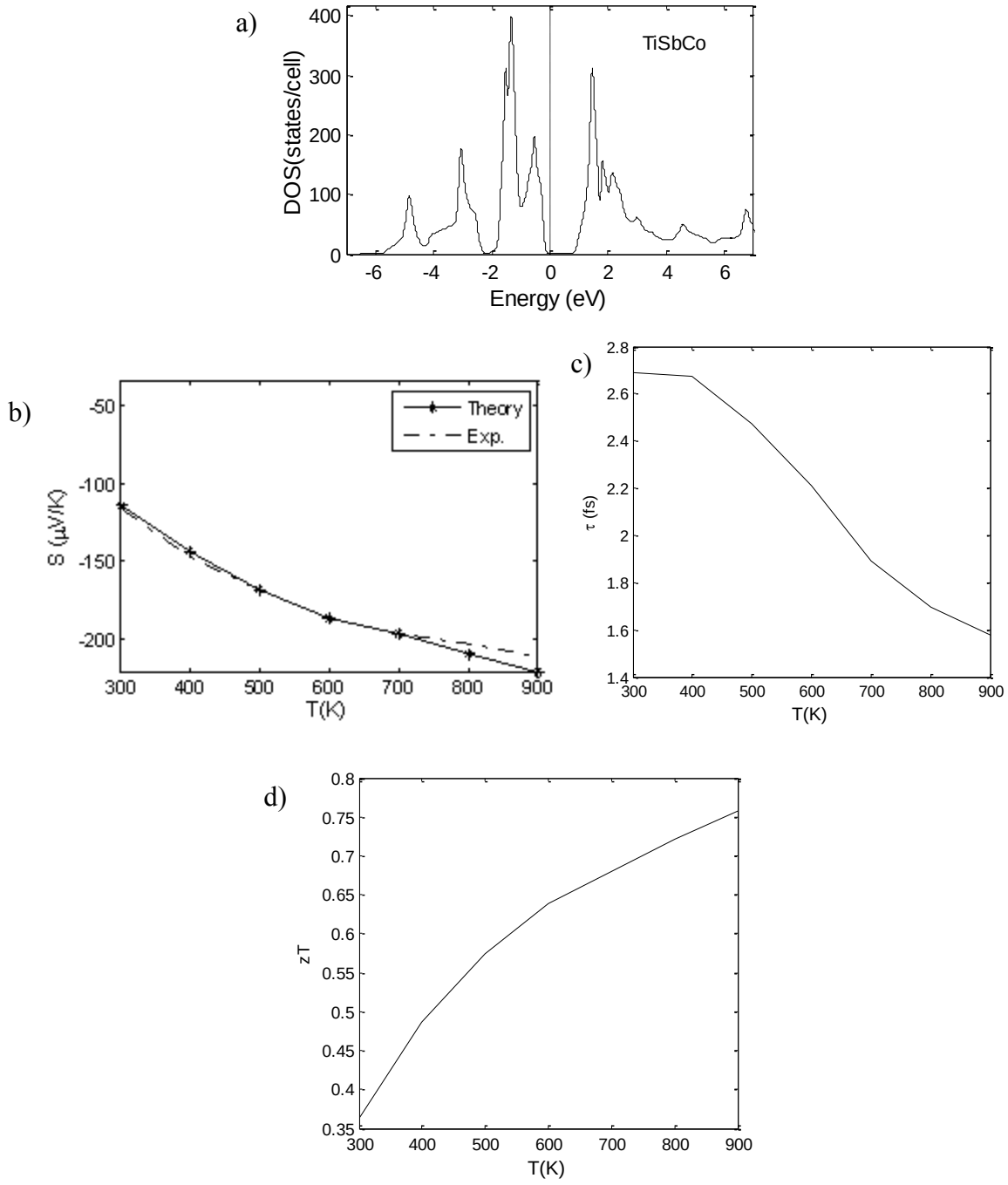

FIG. 2.17. CoSbTi experimental S vs T fit to compute τ and zT. a) DOS, Experimental fit (Fig.b**)** to compute relaxation time **(**Fig.c**)** and zT **(**Fig.d**)**.

NiSnZr

NiSnZr is our first case where the use of LDA along with a fudge-factor "U", is necessary to prevent Mott-insulator[7, 32] behavior (Fig.2.18). The approximate exchange-correlation functional, no doubt, gives reasonable results for ground state energies, but fails in spelling out the proper electronic structure. Metallic behavior of the Half-filled d-shells is the prime reason for such an observation. In such cases, d-d Coulombic energies have to be taken into account and if one adds such a correction, the metallic behavior disappears. Is there a reasonable value of U to be added? Yes! "U", obviously depends on the orbital occupancy which means that the half-filled orbitals have less magnitude of U than the quarter-filled ones. One could make an educated guess and sweep U to match the lattice parameters or the electronic bandgap, OR a single-shot calculation needs the value of U be obtained from XPS[d,e,f]. It is apparent from Fig.2.20 that NiSnZr has a satisfactory max{zT} of 0.7 which agrees with the experimental prediction[31] which predicts maximum zT to be around 0.7.

Computational details: The L(S)DAU parameters used are: U=7.52 and J=0.65. MHP grid of 26^3 was used. The deviation from experimental lattice parameters was close to 1%.

---

[d] This exercise doesn't guarantee exact lattice parameters as there are other shells that suffer from the lack of a better exchange-correlation functional.

[e] Ref. [31] deals with the extraction of U from XPS binding energies. In general, it is the effective (U-J) that needs to be corrected, J being the exchange correction which also depends on the occupancy since the exchange and correlation are a lumped unit in GGA/LDA.

[f] Occupancies needn't always be whole numbers as it would be shown in Chapter III, the electron occupancies may even assume fractional values owing to hybridization of a particular state.

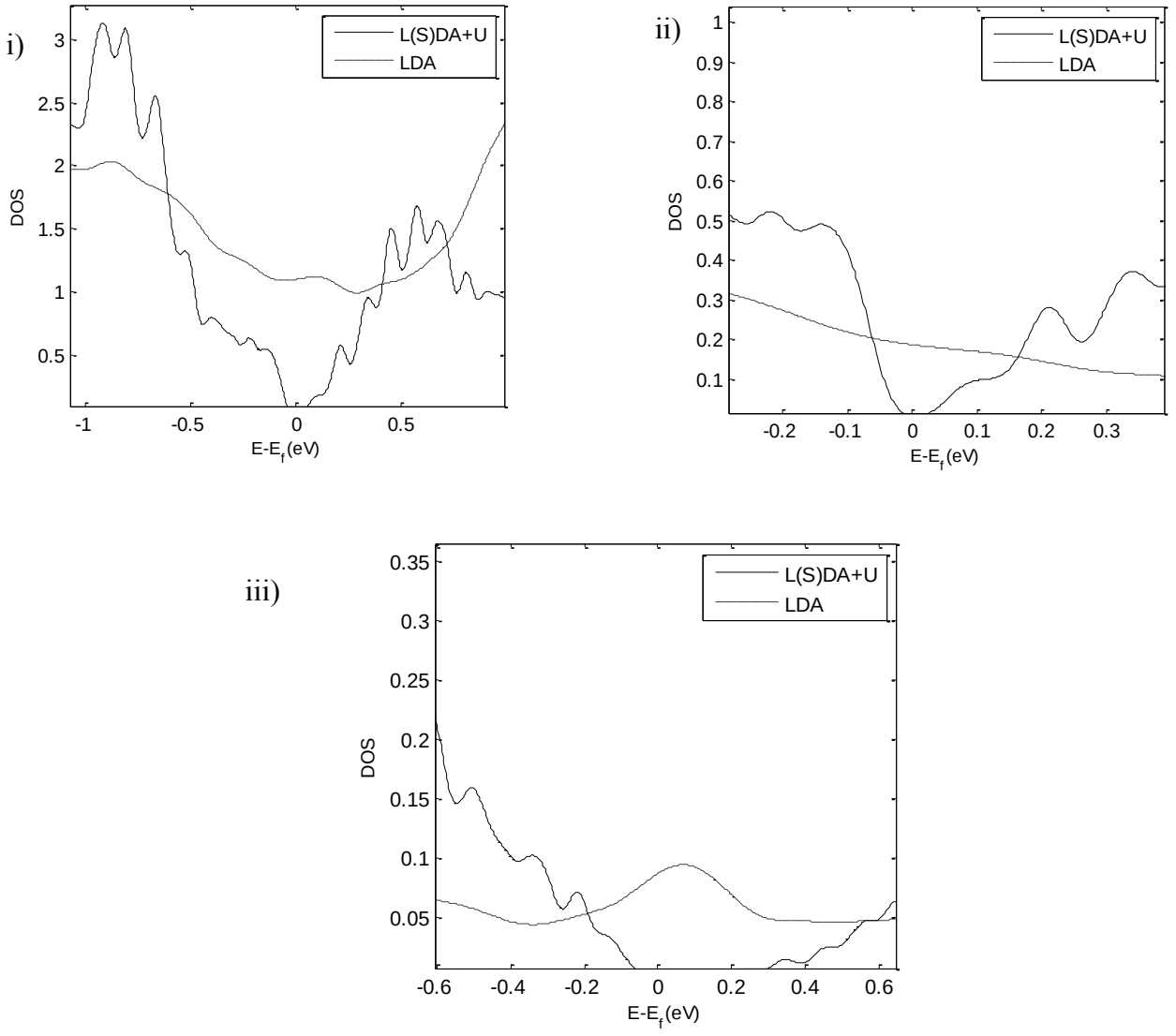

FIG. 2.18. Correlation mistreatment and its effects in NiSnZr. i) Total-DOS of NiSnZr calculated with the two methods – L(S)DA+U (U=7.5, J=0.65) and LDA. Basic implementation of LDA fails to correctly treat correlation effects in highly correlated systems. Figure also compares projected pDOS of Nickel in ii) t_2g and iii) eg states using both methods.

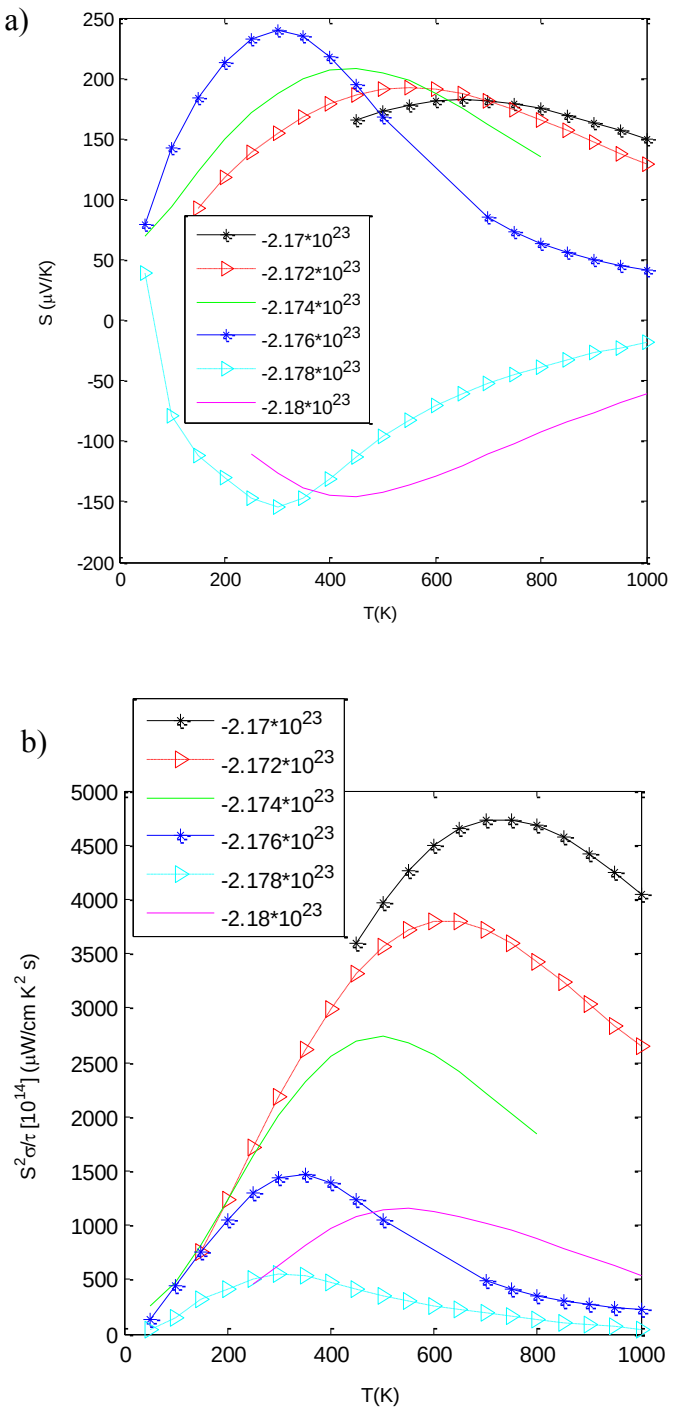

FIG. 2.19. NiSnZr S-T and pf-T curves. a) Seebeck coefficient and b) power factor plots of NiSnZr.

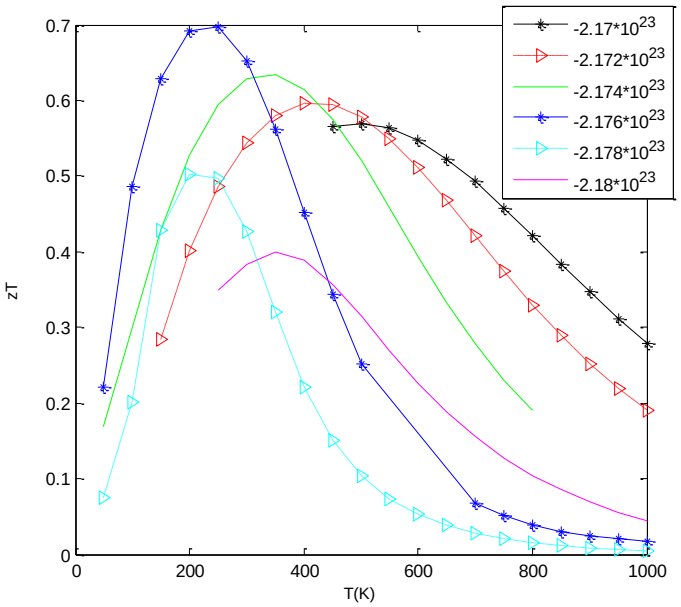

FIG. 2.20. zT vs T plot of NiSnZr.

LaAlSi

Both the power factor and zT are to be kept in mind while deciding the overall performance of a dielectric. Since, Seebeck coefficients occurs as a squared value, one cannot rule out a possibility of a very high Seebeck and very low power factor exists. LaAlSi is a reasonably good thermoelectric for applications below 200 K (Fig.2.21). This is apparent from the mean positions of the various Gaussian like zT vs T curves. At higher T, the electrons get thermally excited and nullify any voltage drop(because of a narrow bandgap).

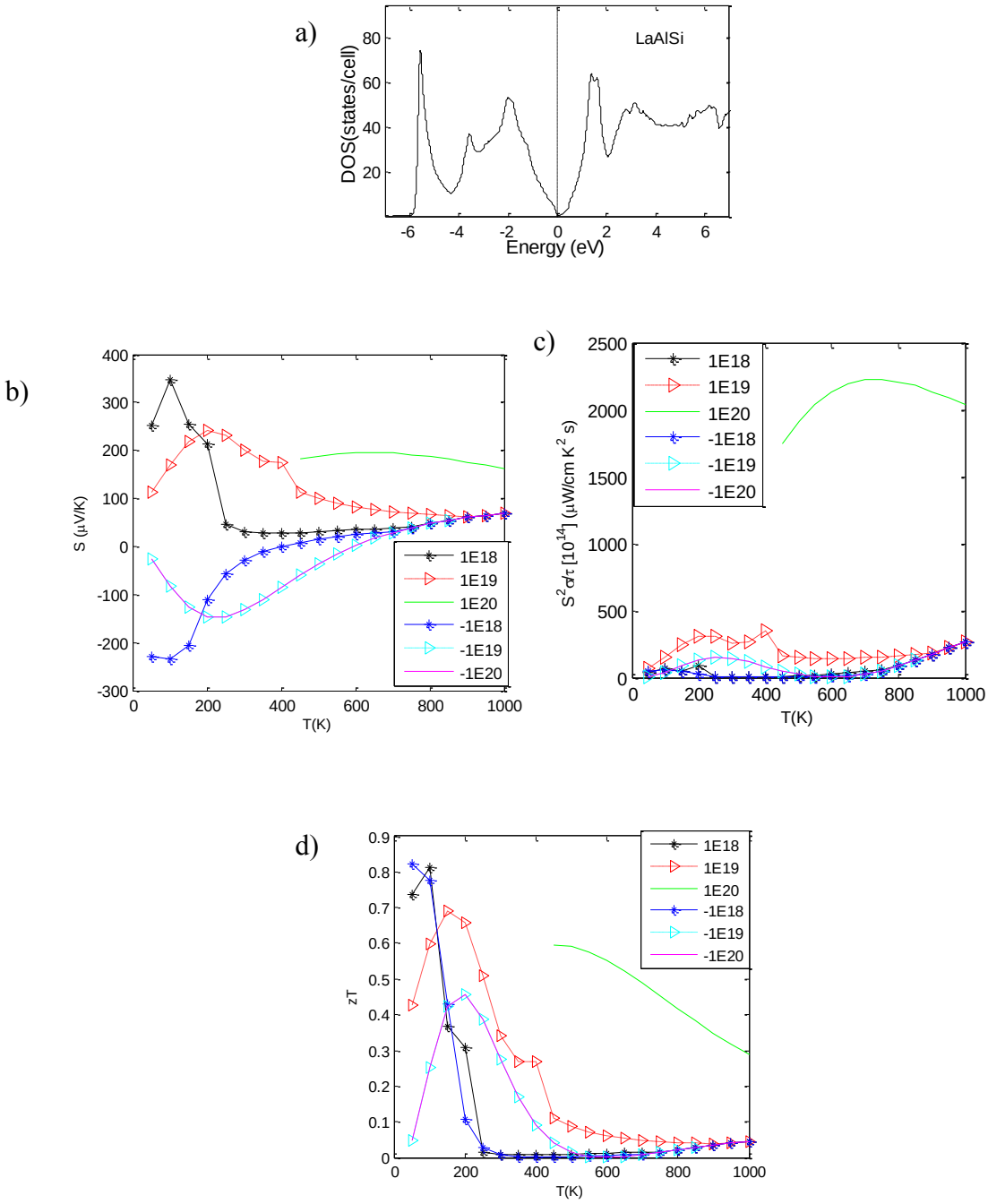

FIG. 2.21. TE performance metrics of LiAlSi. a) DOS , b) Seebeck coefficient , c) power factor and d) zT plots of LiAlSi.

NbFeSb

Suprisingly, NbFeSb shows a good thermoelectric behavior for temperatures below 600K (Fig.2.23-2.24). There was minimal deviation in the calculated structural parameters when compared to the experimental ones obtained from ICSD. The bandgap was found to be 0.075 eV (Fig.2.22). A maximum zT was found to be 1.14. Bandgap being small, it is possible for even the faintest of temperature gradients to populate the conduction band (which has a sharp band edge). Since the conduction band electrons are massive (from the DOS) and delocalized, it possibly develops reasonable potential drop (as is it proportional to the effective mass) and also has high-conductivity.

Computational details: There was minimal deviation between the experimental and the computed lattice parameters. LDA was used for both the exchange and correlation functional. 18^3 MHP grid was used from an SCF calculation which followed a 8^3 MHP relaxation[g].

Statement without proof: The difference between computed lattice parameters and the experimental values is minimal if one uses a primitive cell representation instead of the supercell.

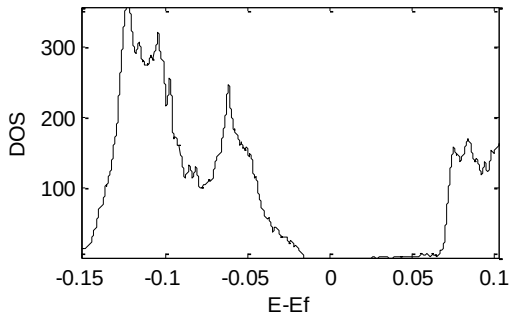

FIG. 2.22. DOS plot of NbFeSb.

[g] Prior to calculating the SCF data values, all structures were checked for convergence (1 meV) on the k-points and the total energy.

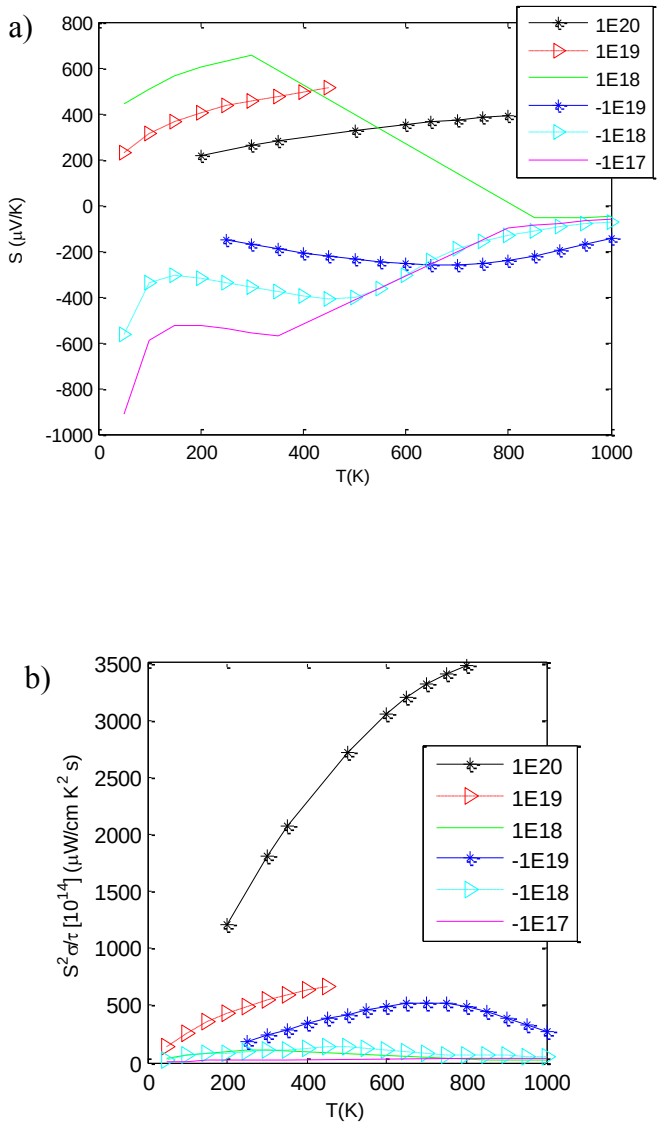

FIG. 2.23. NbFeSb S-T and pf-T curves. a) Seebeck coefficient and b) power factor plots of NbFeSb.

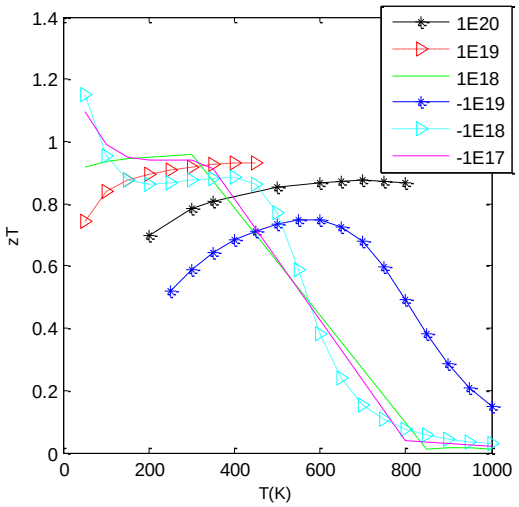

FIG. 2.24. zT vs T plot of NbFeSb.

2.3 Perovskites

Structures having ABO_3 arrangement (Fig.2.25) with A atoms sitting on the corners of the cube, B at the BCC and O's occupying the FCC positions, are classified as Perovskites. Being oxides, they behave as good dielectrics and have potential applications as high-zT-thermoelectrics. Perovskite structures usually have electrons with a large effective mass (close to $10m_0$)[33] which is a direct indication of its high Seebeck coefficient. The thermal conductivities of these ceramics are usually very high (for $BaTiO_3$(BTO)-8.5 W m^{-1} K^{-1} and for $SrTiO_3$(STO)~10 W m^{-1} K^{-1}). However, like in the Si-Ge alloys, alloys of solid-solutions of BTO and STO have disorder scattering, thereby tremendously reducing the value of thermal conductivity. Since we are interested in just the electronic contribution, we neglect k_l assuming it to be minimum. Lanthanum Cobaltate (*also a Perovskite*)-dealt as a special case in Chapter III, shows a peculiar behavior. There are multiple spin phases of $LaCoO_3$. Estimating Seebeck coefficient could be difficult when phase transitions occur. We, however, outline a simple procedure to compute the Curie temperature and also the thermoelectric parameters, thereof. The structure $CaSiO_3$ shows a good room temperature thermoelectric behavior with a zT_{max} of almost unity.

STO and BTO

As with the case of NiSnZr, half-filled d-shells suffer from drastic reduction in bandgaps. We used L(S)DA+U, STO:U=4.844,J=0.92 and BTO:U=4.71,J=0.90 (values obtained by XPS comparison) to include strong correlation effect and obtain bandgap as shown in Fig.2.26. In the case of STO, the doping concentration is high (0.6E21) due to the unconventional experiment employing a *p-type* dopant[34]. This configuration fares well at 1000 K (Fig.2.27-2.29; Fig.2.30-Fig.2.31) where a zT_{max} with S=305 μV/K, is found to be around 0.85.

Computational details: A 25^3(15625) MHP reciprocal space grid is used. PBE is used for xc. The band gap was found to be about 3.2 eV matching the experimental value.

Strontium Titanate ($SrTiO_3$)

Experimental

Structure: cubic

[a b c]: 3.99

Bandgap: 3.2 eV

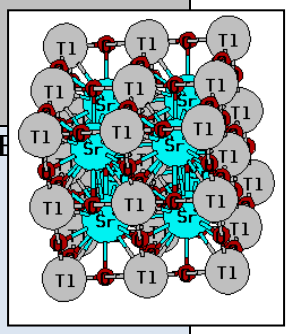

DFT (PBE

Energy Cutoff: 550

[a b c]: 3.95

Bandgap: 3.2 eV

K-Points: 15625

Maximum zT: 0.99 at T>200 K

Atoms: 5

Lanthanum Cobaltate ($LaCoO_3$)

Experimental

Structure: trigonal

[a b c]: 3.82

Bandgap[16]: 0.28 eV

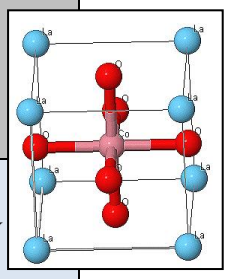

DFT (GGA+U)

Energy Cutoff: 800 eV

[a b c]: 3.63

Bandgap: 0.32**,** 1.1 eV

K-Points: 5832

Maximum zT: 0.8 for T above 400K

Atoms: 10

Barium Titanate ($BaTiO_3$)

$BaTiO_3$-Experimental

Structure: tetragonal

[a b c]: 4

Bandgap: 3.2 eV

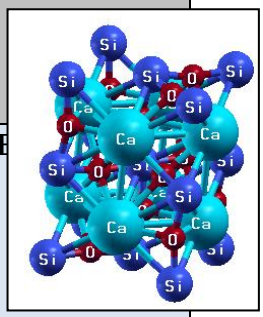

DFT (PBE

Energy Cutoff: 500

[a b c]: 4.04

Bandgap: 3.2 eV

K-Points: 15625

Maximum zT: 0.8 for T>200 K

Atoms: 5

Model H

Calcium Silicate ($CaSiO_3$)

$CaSiO_3$-Experimental

Structure: orthorhombic

[a b c]: 4.48 6.31 4.54

Bandgap:

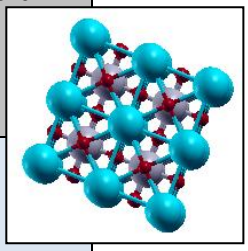

DFT (GGA)

Energy Cutoff: 1200

[a b c]: 4.48 6.31 5.11

Bandgap: 0.27 eV

K-Points: 1000

Maximum zT: 1 for T > 300K

Atoms: 20

FIG. 2.25. Summary of lattice parameters, computational parameters, and band gaps in Perovskites.

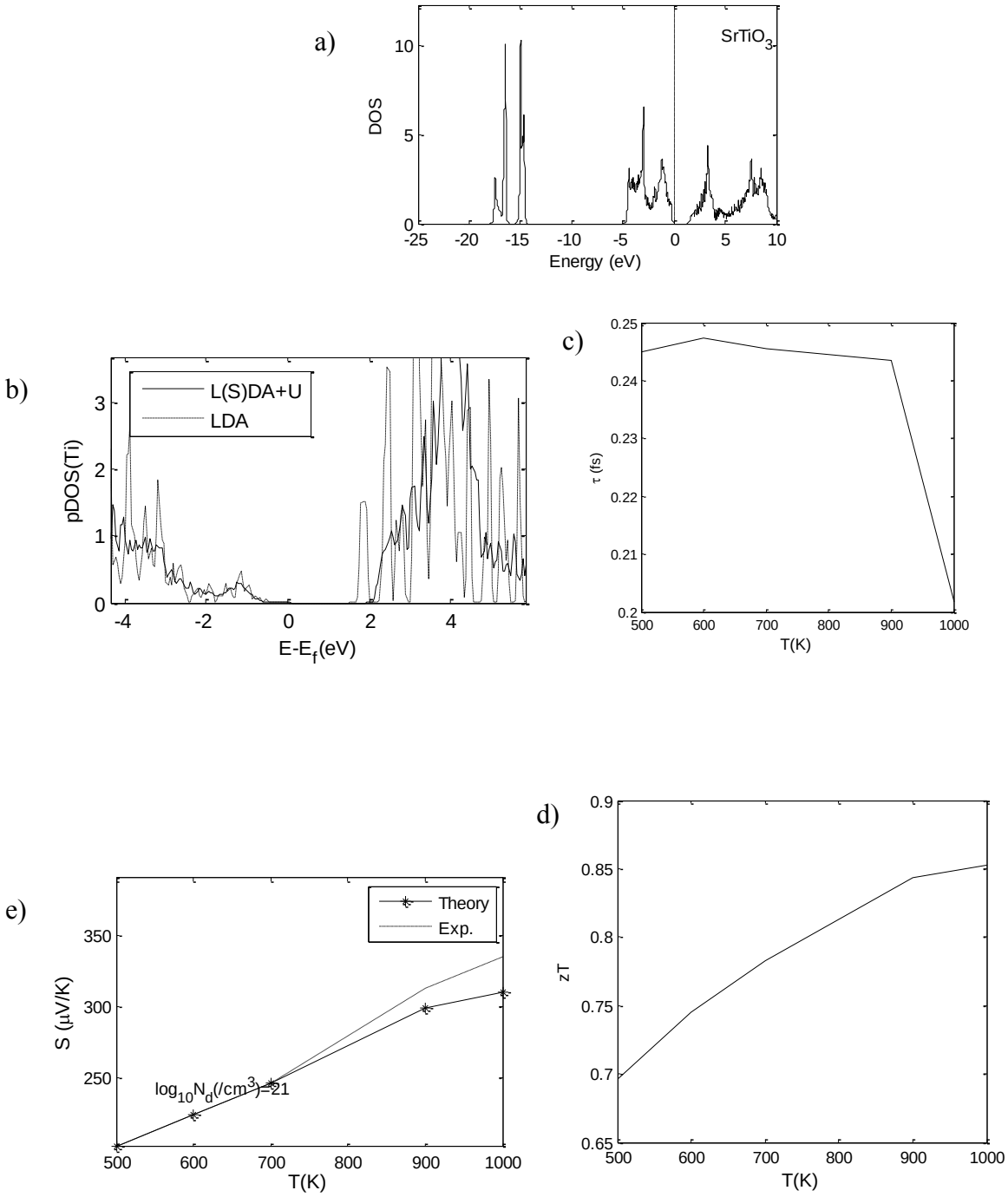

FIG. 2.26. STO electronic structure and experimental S-T fits to extract τ and zT. DOS [fig.a] , partial DOS (LDA, L(S)DAU) [fig.b], relaxation time [fig.c] vs temperature, zT [fig.d], Seebeck coefficient [fig.e] fit to experiment.

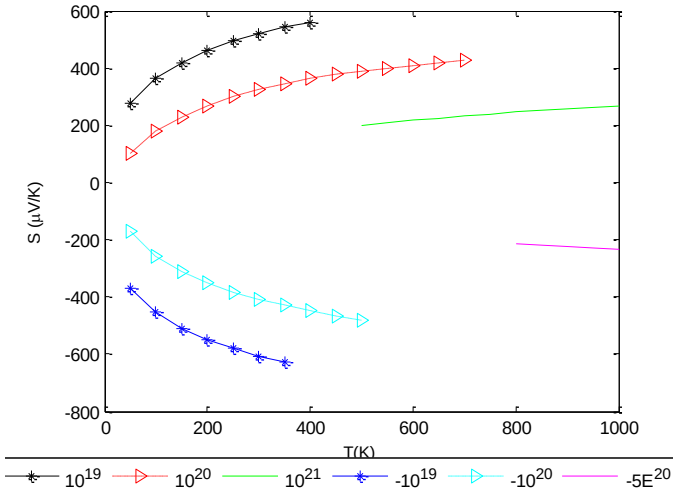

FIG. 2.27. STO S-T curves. Negative legend values imply n-type doping.

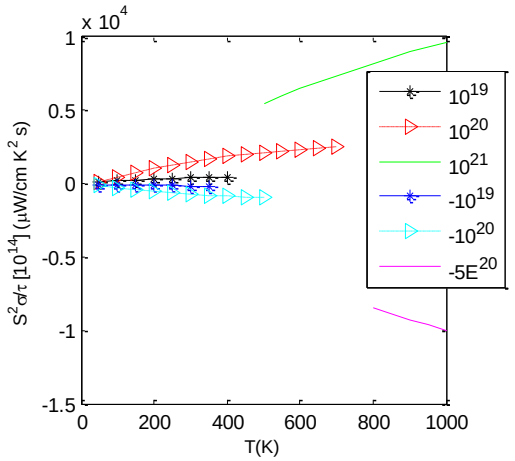

FIG. 2.28. Estimated power factor values of STO.

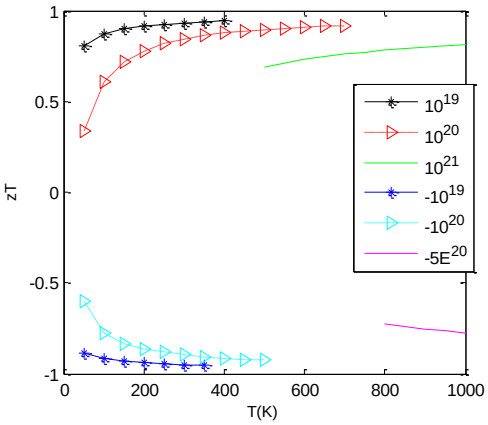

FIG. 2.29. STO zT plots for various doping concentrations. STO fares better at high temperatures.

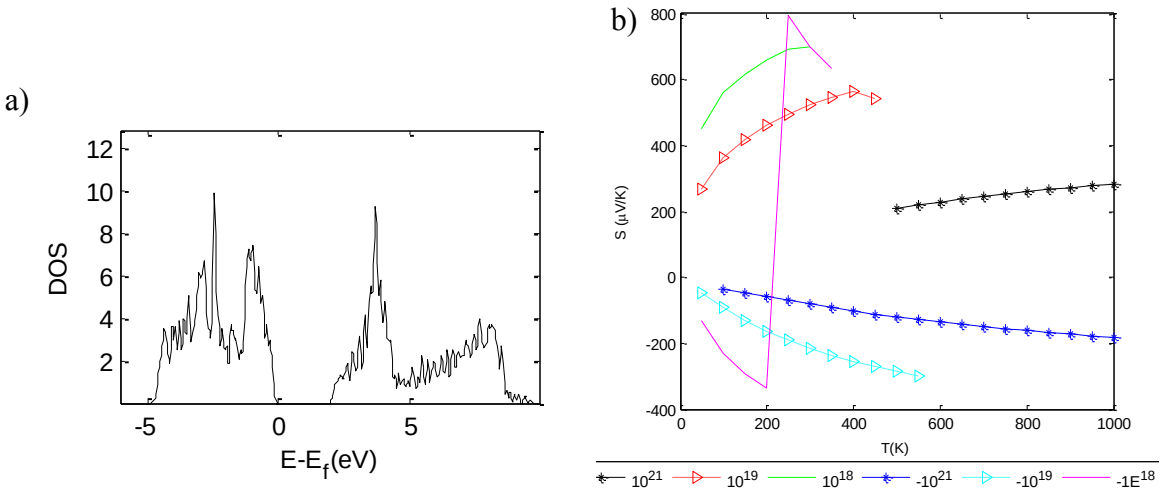

FIG. 2.30. BTO DOS and S-T plots. **a)** DOS and **b)** Seebeck coefficient plots of $BaTiO_3$.

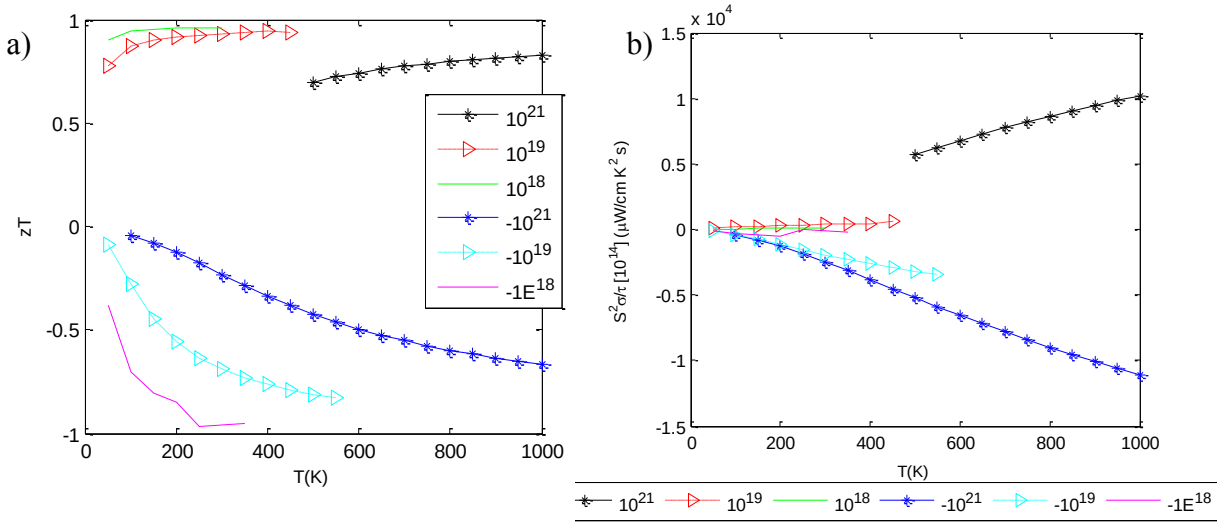

FIG. 2.31. BTO pf-T and zT plots for various doping concentrations. **a)** power factor and **b)** zT plots of $BaTiO_3$.

$CaSiO_3$

For the same concentration, (ref. Fig.2.32), p-type $CaSiO_3$ fares better than the n-doped structure. It boasts of a good power factor and a moderate-to-good Seebeck coefficient. The maximum zT was found to be 1.05 (Fig.2.32) at room temperature and was found to be independent of carrier concentration in the p-type $CaSiO_3$. Clearly, since the conduction band-edge implies a lighter effective mass, though the mobility is high, it is prone to scattering. No experimental data on the thermal conductivity of the perovskite phase of $CaSiO_3$ is available. But oxygen rich Perovskite structures have a good thermal conductivity.

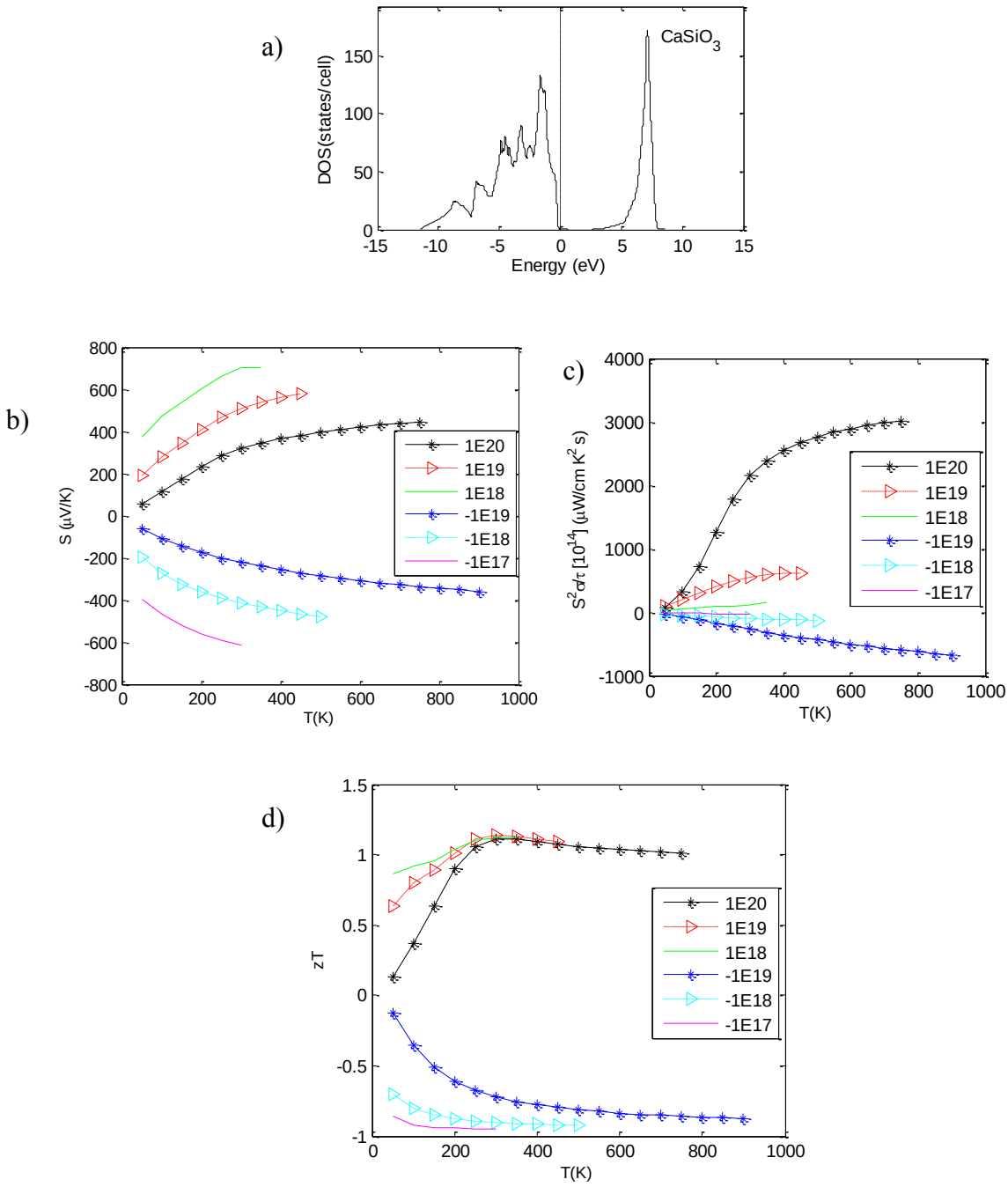

FIG. 2.32. CaSiO3 electronic structure and TE performance metric plots at various doping concentrations. a) DOS, b) Seebeck coefficient, c) power factor and d) zT plots of $CaSiO_3$.

2.4 Assorted Class of Thermoelectrics

Please refer Fig.2.33 for a list of crystal structures under this category and their TE performance.

ZnO

Figures Fig.2.34 and Fig.2.35 highlight the concentration specific moderate-to-high power factor of ZnO. zT also appears to be high for all temperatures (Fig.2.35). However, experimentally, the k_l is again found to have dominance in limiting zT. k_l has an average value of 50 W/m·K which is too huge a value to neglect (there is a faint hope that bandstructure engineering or alloying would bring k_l down). Hence ZnO turns out to be a bad thermoelectric. Experimental observations were fit (Fig.2.34) and the doping density was found to be 4.067e+018. Pf, and zT were obtained by fitting SvsT, extracting τ vs T for the same and computing pf and zT.

Computational details: of ZnO and $FeSi_2$: PBE functional was used for both exchange and correlation. In the case of ZnO, the deviation in the structural parameters to one obtained experimentally was found to be 4% while $FeSi_2$ had a meager 0.5%. 20^3 MHP grid was used for ZnO and 28^3 for $FeSi_2$.

$FeSi_2$ and FeSi

FeSi being a narrow bandgap semiconductor (Fig.2.36, Fig.2.37) isn't a good candidate for thermoelectric applications. Hence, only partial results are presented and others suppressed. $FeSi_2$ on the other hand exists in two phases α-$FeSi_2$ and β-$FeSi_2$. β-$FeSi_2$ is a low temperature phase (for temperature less than 1200 K) which happens to be within the bounds of applicability and of our interest. β-$FeSi_2$ shows a bandgap of 0.8 eV (Fig.2.38) which is in close acceptance with the experimental result. Orthorhombic in structure, it belongs to D182h space group. However, as with all the crystals, even $FeSi_2$ has the k_l problem. However, alloying with Co halves the k_l to ~ 4 W/m·K without much affecting the electronic properties. It has an exceptional power factor and is applicable for below room temperature operations (as it is apparent from SvsT curves Fig.2.39). The flat bands at the valence and the conduction edges are a result of the heavy Fe d electrons which also happens to open up the bandgap.

$FeSi_2$	
Experimental	
Structure: orthorhombic	
[a b c]: -6.23 6.23 7.81	
Bandgap[16]: 0.78 eV	
DFT(PBE)	
Energy Cutoff: 400 eV	
[a b c]:6.187 6.187 7.688	
Bandgap[35]: 0.8 eV	
K-Points: 21952	
Maximum zT: 1 above 200K	
Atoms: 24	

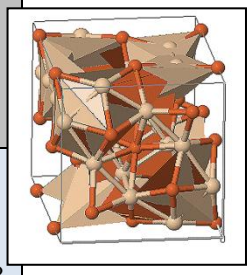

FeSi	
Experimental	
Structure: cubic	
[a b c]: 4.45	
Bandgap[16]: 0.28 eV	
DFT(PBE)	
Energy Cutoff: 400 eV	
[a b c]: 4.45	
Bandgap: 0.1 eV	
K-Points: 15625	
Maximum zT: 0.9 at 150K	
Atoms: 8	

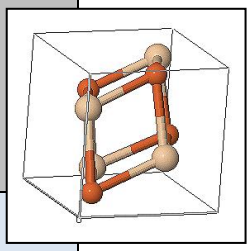

Zinc Oxide (ZnO)	
Experimental	
Structure: hexagonal	
[a b c]: 3.25 3.25 5.20	
Bandgap[16]: 3.1 eV	
DFT(PBE)	
Energy Cutoff: 300 eV	
[a b c]: 3.28 3.28 5.32	
Bandgap: 3.2 eV	
K-Points: 8000	
Maximum zT: 1 above 200K	
Atoms: 4	

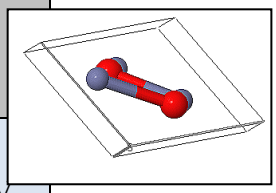

FIG. 2.33. Summary of lattice parameters, computational parameters, and band gaps of the assorted class of thermoelectrics.

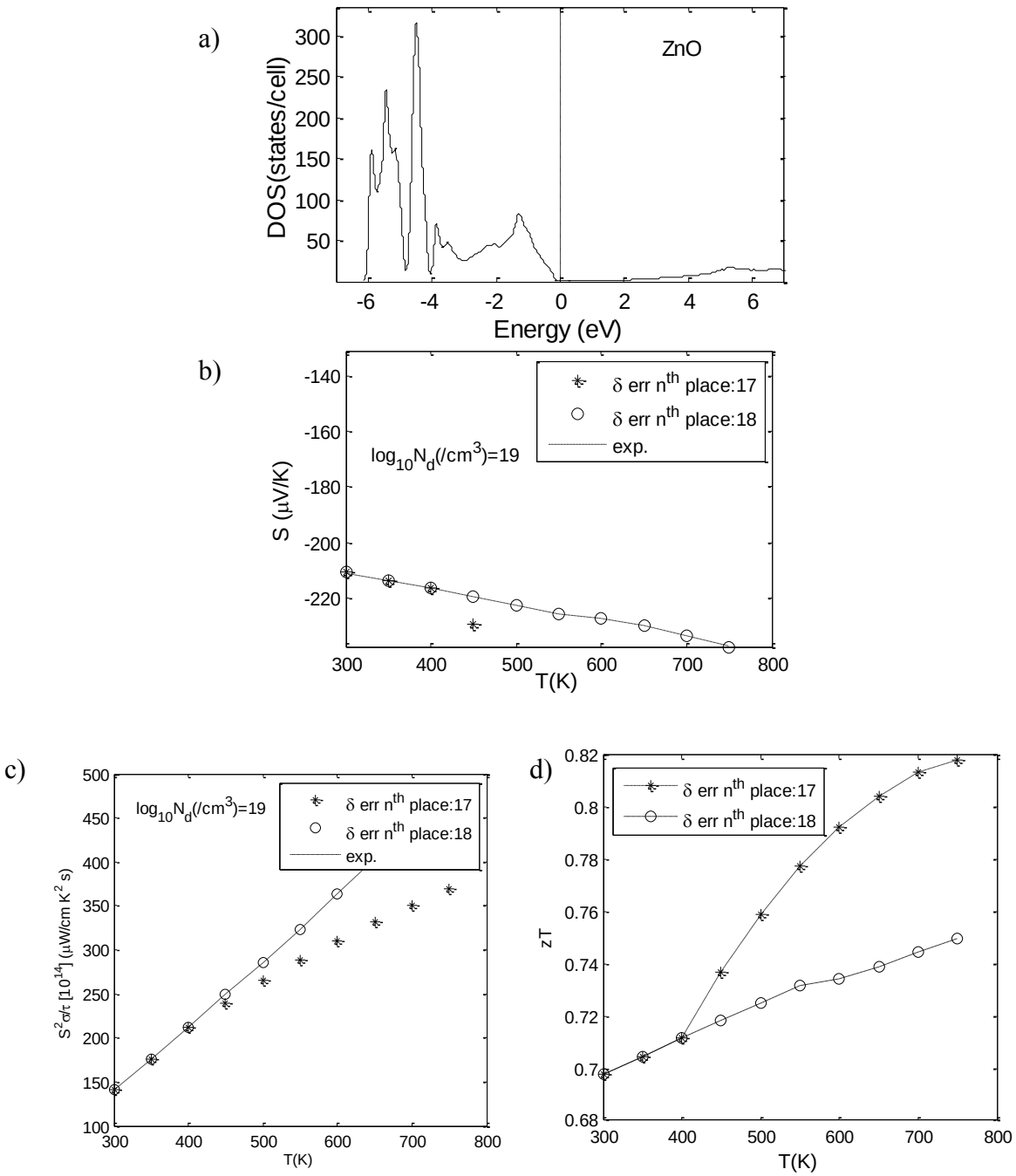

FIG. 2.34. Electronic structure and TE performance plots of ZnO. a) DOS , b) Seebeck coefficient, c) power factor and d) zT plots of ZnO fit to experiments. The doping concentration was found to be -4E18.

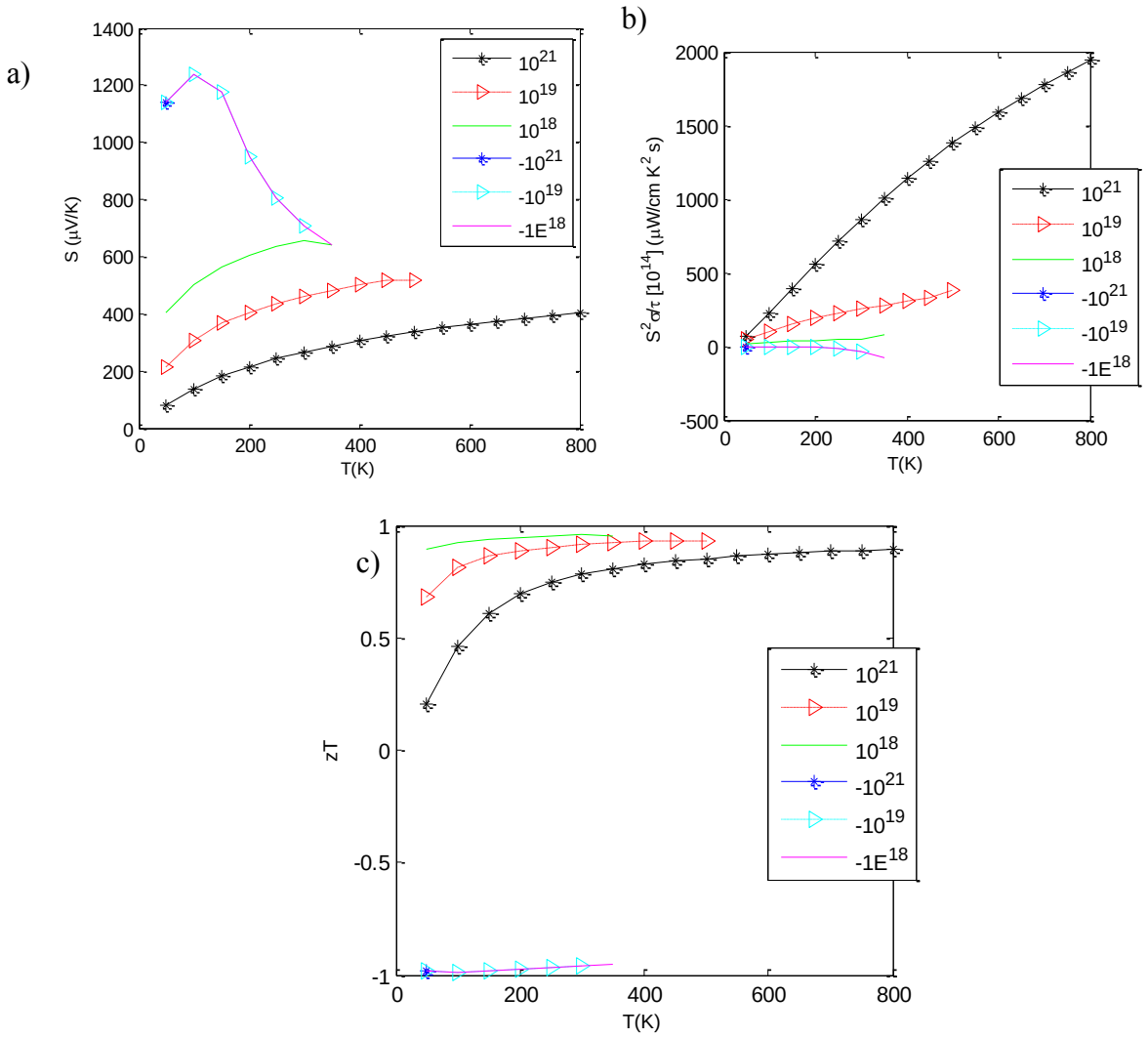

FIG. 2.35. ZnO S-T, pf-T and zT plots. a) Seebeck coefficient, b) power factor and c) zT plots of ZnO.

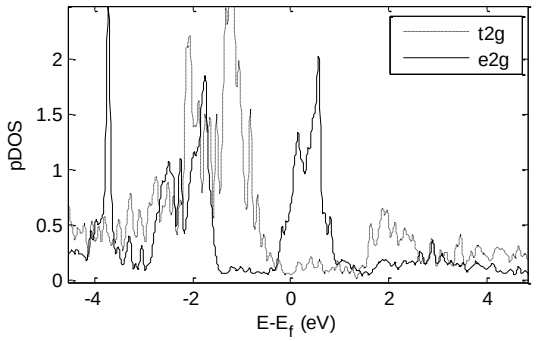

FIG. 2.36. Mott-insulator behavior in FeSi. FeSi is a narrow gap semiconductor. As it has now become apparent that half-filled highly correlated systems behave as Mott insulators, unless the t_2g and the eg aren't explicitly handled, the system would remain conductive.

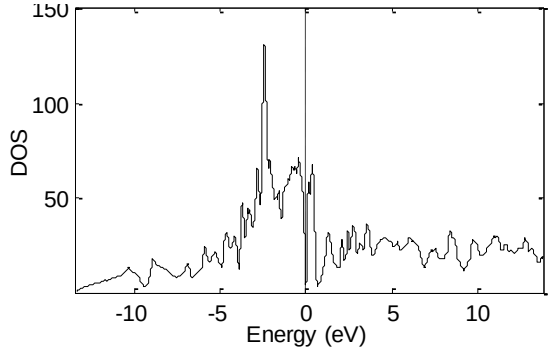

FIG. 2.37. FeSi DOS plot.The band gap being close to 0.01 eV.

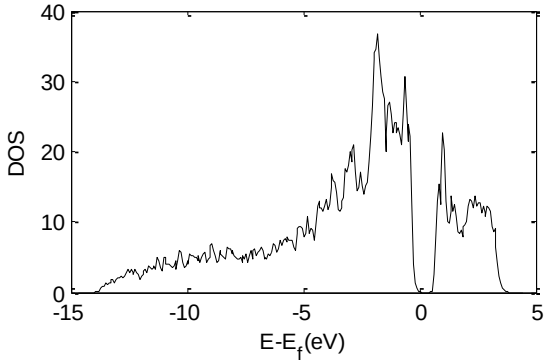

FIG. 2.38. β-$FeSi_2$ DOS plot. β-$FeSi_2$'s calculated bandgap value of 0.8 eV in close comparison to the experimental direct band gap value of 0.85 eV[36].

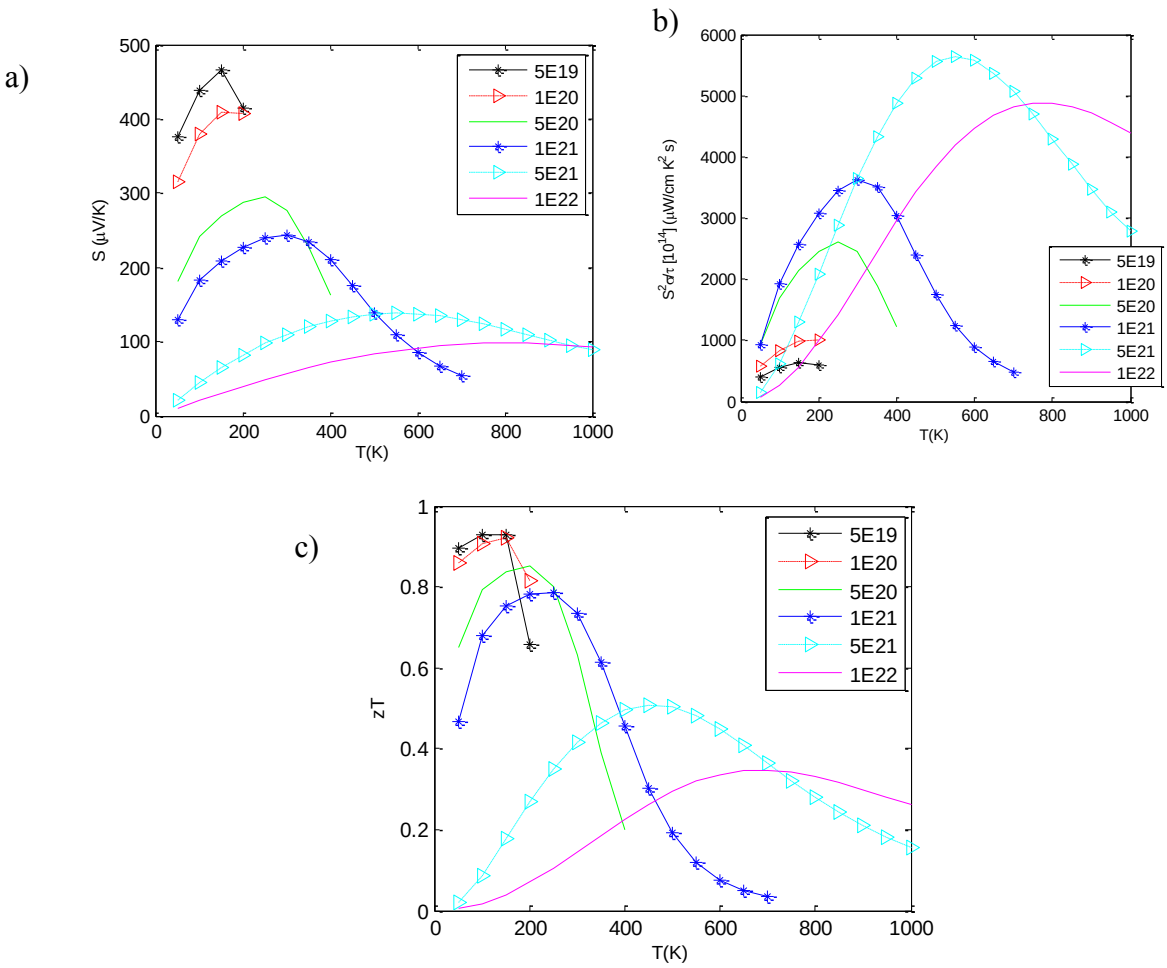

FIG. 2.39. β-$FeSi_2$ S-T, pf-T and zT plots. a)Seebeck coefficient, b)power factor and c) zT plots of $FeSi_2$.

2.5 Clathrates and Skutterudites

Filled skutterudites and Clathrates (Fig.2.40) are promising candidates for high zT thermoelectric designs. Filled skutterudites have the form RM_4X_{12} where R is a rare earth or the Rattler, M is a metal, and X is a pnicogen (P, Sb, As). Pnicogen atoms form rings. The pnicogen rings encapsulate the metal M forming an octahedral. There are two cages per unit cell leaving two voids that could be filled. There is also an icosohedron formed by the 12 pnicogen atoms, each of which holds the non-bonded atom (like Sb) at its center. The cage size depends on the pnicogen used and increases as one moves down the pnicogen group. The pnicogen atoms are well coordinated and hence do not form bonds with "R". Hence the "R" atom rattles and scatters

phonons thereby decreasing the lattice thermal conductivity. And with the missing rattler, one has a pure *unfilled* skutterudite and the phonon modes come back. They assume the Im3 crystal structure. The electronic structure of filled skutterudites is explained using Zintl electronegativity theory[37] which proves that the filled skutterudite configurations are semiconducting.

$SrFe_4Sb_{12}$

As guessed correctly by the Zintl theory, $SrFe_4Sb_{12}$ is a semiconductor with a bandgap of 0.6eV (Fig.2.41). Doping has a good effect on the Seebeck coefficient. $SrFe_4Sb_{12}$ offers excellent power factors (Fig.2.41) and reasonably good Seebeck coefficients (Fig.2.41). n-type doping concentration of 6E21 has appreciable zT at 800-1000K operation. We predict better thermal conductivity when Sr is replaced by Ba.

*Computational details:*There is a 0.4% deviation in the calculated structural parameters. 12^3 MHP grid was used.

$CoSb_3$

$CoSb_3$ is a narrow bandgap semiconductor (Fig.2.42). It is not as good a phonon glass as the filled skutterudite, but has very good Seebeck coefficients and power factors (Fig.2.43). SvsT curves are fit to experiment (Fig.2.42). We predict the doping concentration to be around 3E18 /cm^3. The scattering time is also plotted versus temperature. $CoSb_3$ has a wide operating range between 200-800K depending on the concentration of the dopant.

Computational details: There is a 2% deviation in the lattice parameters. 18^3 MHP grid was used for the SCF calculation on the optimized geometry.

Cadmium Carbide

Experimental
Structure: cubic
[a b c]: -
Bandgap[16]: 0.28 eV

DFT(PBE)
Energy Cutoff: 950 eV
[a b c]: 9.21
Bandgap: 4.98 eV
K-Points: 5832
Maximum zT: 0.24 at 400K
Atoms: 2

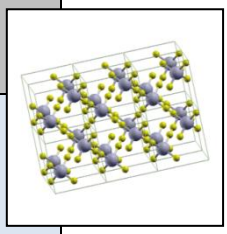

Strontium Ferrous Antimonide ($SrFe_4Sb_{12}$)

Experimental (PBE)
Structure: cubic
[a b c]: 9.18
Bandgap: -

DFT
Energy Cutoff: 500 eV
[a b c]: 9.21
Bandgap: 0.6 eV
K-Points: 1728
Maximum zT: 0.8 for T between 800 K to1000 K

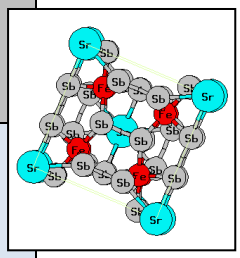

Model J

Cadmium Cyanide ($Cd(CN)_2$)

Experimental
Structure: cubic
[a b c]: 6.32
Bandgap[16]: 0.28 eV

DFT(PBE)
Energy Cutoff: 900 eV
[a b c]: 6.46
Bandgap: 5.82 eV
K-Points: 5832
Maximum zT: 1 over all T
Atoms: 48

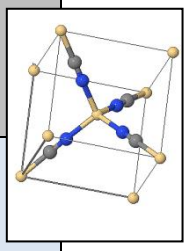

Cobalt Antimonide ($CoSb_3$)

Experimental
Structure: cubic
[a b c]: 9.04
Bandgap[16]: 0.28 eV

DFT(GGA)
Energy Cutoff: 500 eV
[a b c]: 9.21
Bandgap: 0.43 eV
K-Points: 5832
Maximum zT: 0.8 for T over 1000K
Atoms: 2

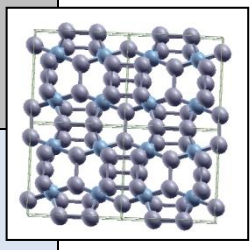

FIG. 2.40. Summary of lattice parameters, computational parameters, and band gaps in Clathrates and Skutterudites.

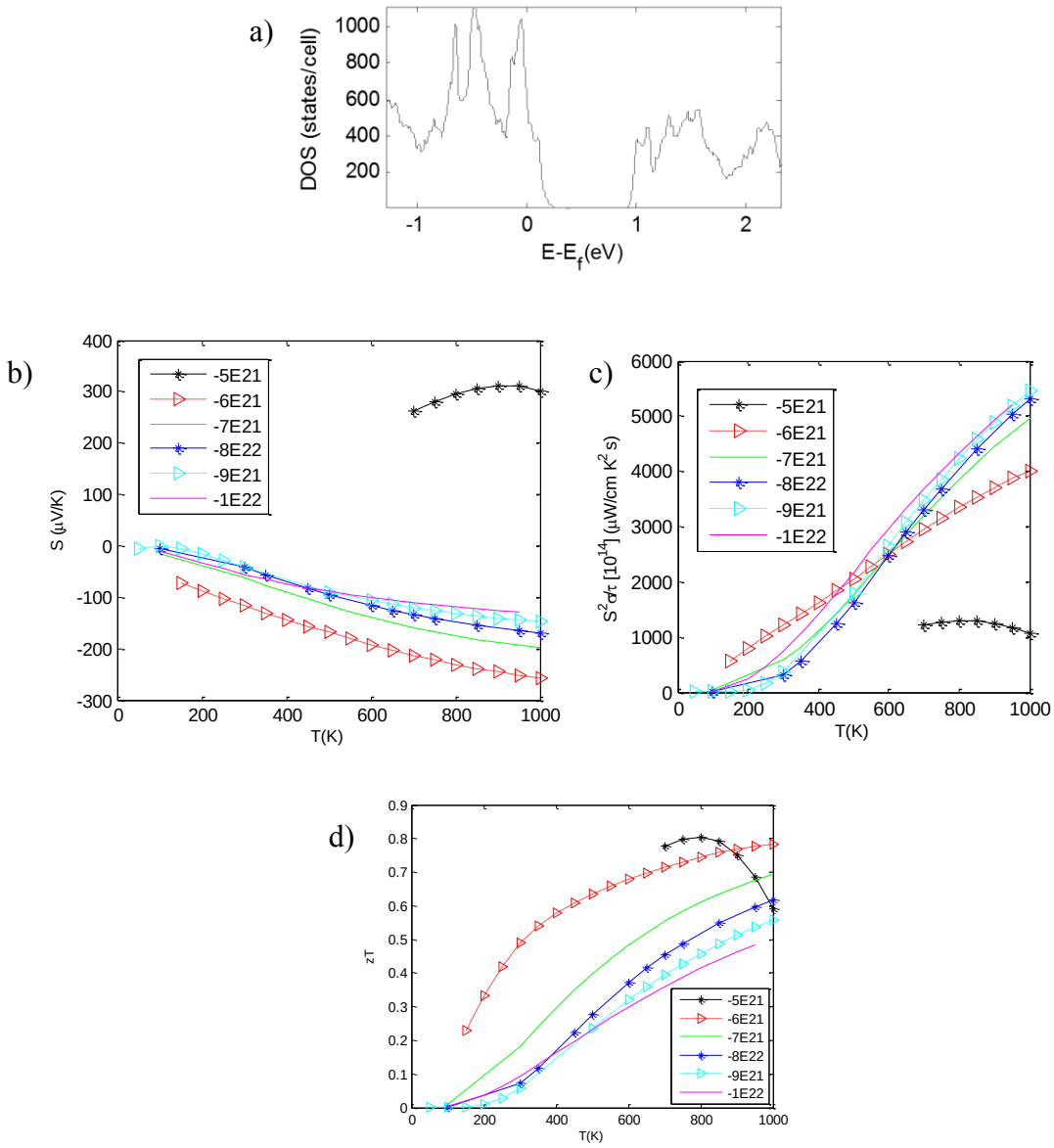

FIG. 2.41. Electronic structure and TE performance of $SrFe_4Sb_{12}$. a) DOS, b) Seebeck coefficient, c) power factor and d) zT plots of $SrFe_4Sb_{12}$.

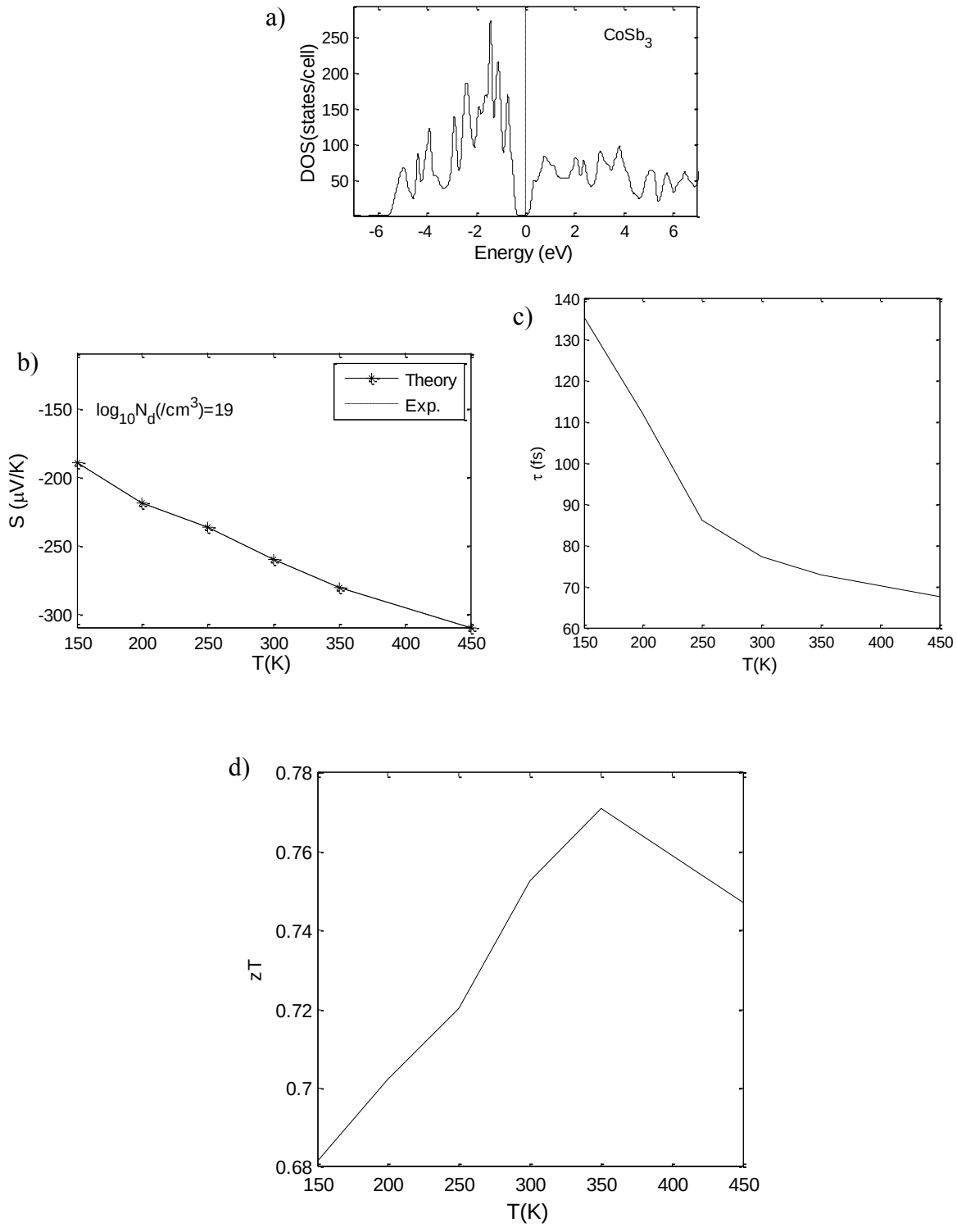

FIG. 2.42. Unfilled $CoSb_3$ electronic structure and S-T experimental fits to compute τ-T and zT. a) DOS, Seebeck coefficient, power factor and zT plots (b-d) of $CoSb_3$ fit to experiments.

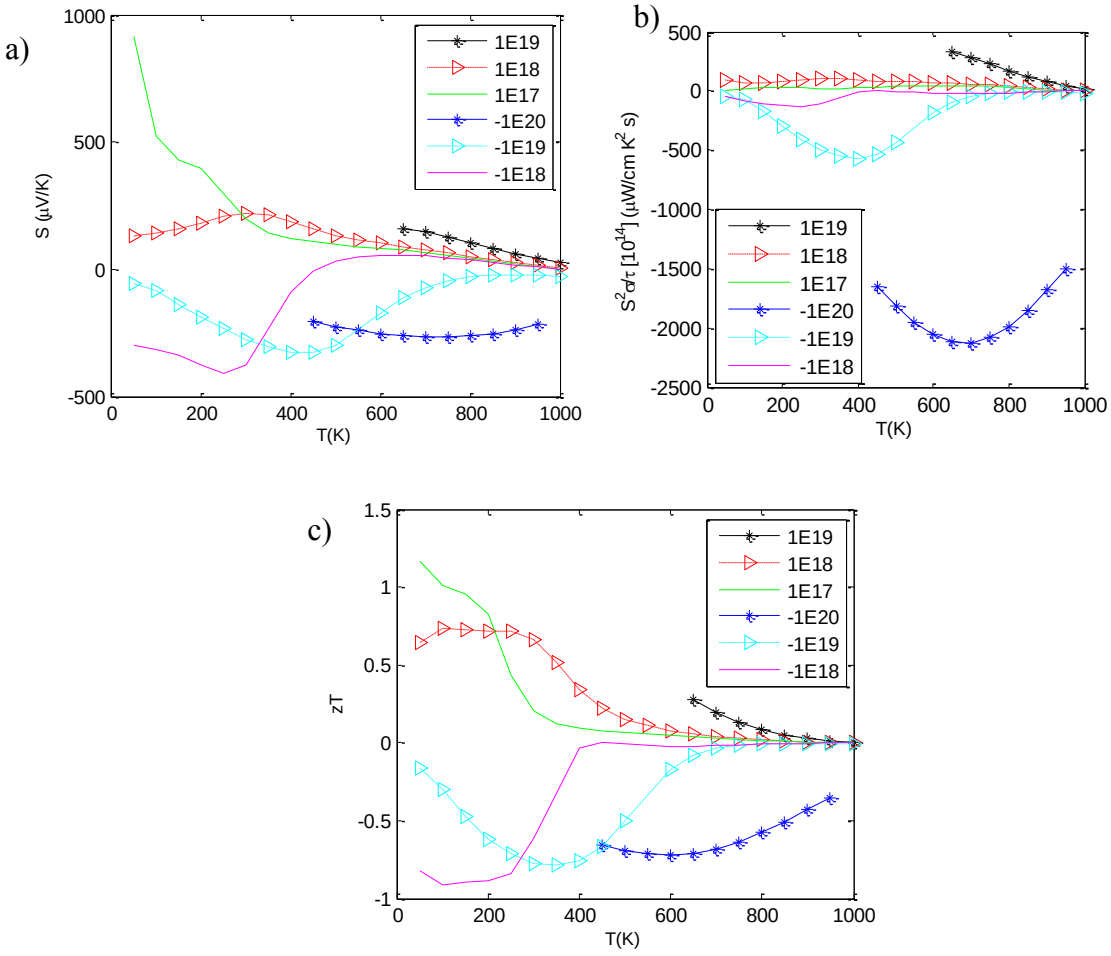

FIG. 2.43 $CoSb_3$ TE performance plots at various doping concentrations. a) Seebeck coefficient, b) power factor and c) zT plots of $CoSb_3$.

$Cd(CN)_2$ and CdC_2

The overwhelming size of the clathrate cages and the minimal symmetry makes it difficult to perform first principle calculations (ref. Table 2.1). Cadmium Carbide and Cadmium Cyanamide are simplest of clathrates. Clathrates also occur naturally (for eg. Methane Clathrates). But, however, the naturally occurring clathrates may not be an ideal candidate for direct use. And hence one needs nanostructuring techniques to design and process clathrates. Cadmium Cyanamide is a wide bandgap (Fig.2.44) and a natural p-type semiconductor with a bandgap of

6.32 eV. But one notes from the power-factor curves that the conductivity is minimal although the thermoelectric efficiency magnifies the overall effect. But, it acts as a good thermoelectric, applied to operating temperatures of over 200 K (Fig.2.45). CdC2 is another example of a bad insulator. With Fermi being penetrating the valence band, decreases zT (Fig.2.46).

TABLE 2.1. Comparison of wall times between Clathrates and highly-symmetric Chalcogenides.

Element	**Processors**	**Wall time (Seconds)**
$Cd(CN)_2$	16	152513(42.36 h)
PbSe	16	71

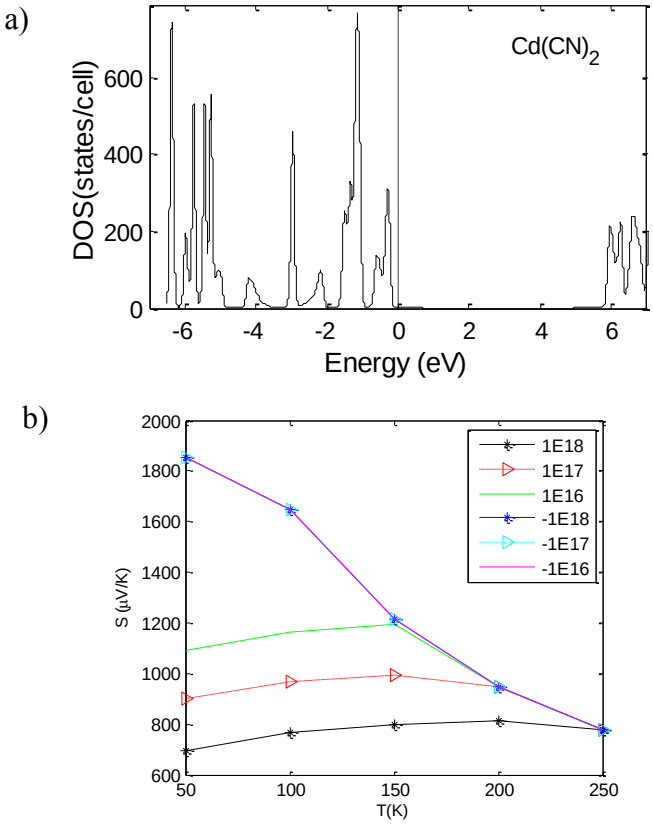

FIG. 2.44. $Cd(CN)_2$ DOS and S-T plots. a) DOS and Seebeck coefficient plots of $Cd(CN)_2$.

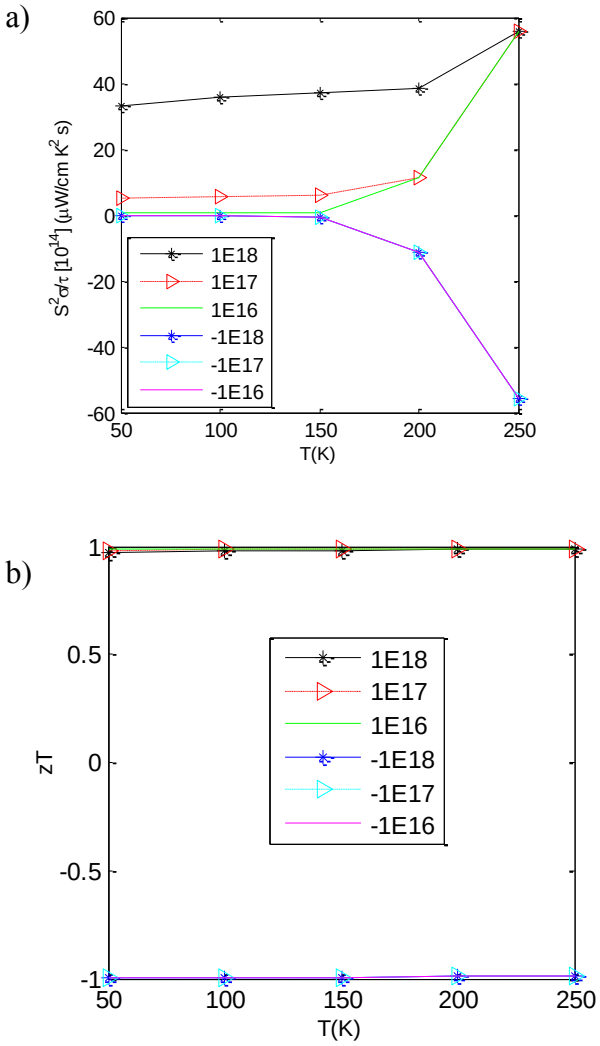

FIG. 2.45. $Cd(CN)_2$ pf-T and zT curves at various doping levels. a) power factor and b) zT plots of $Cd(CN)_2$.

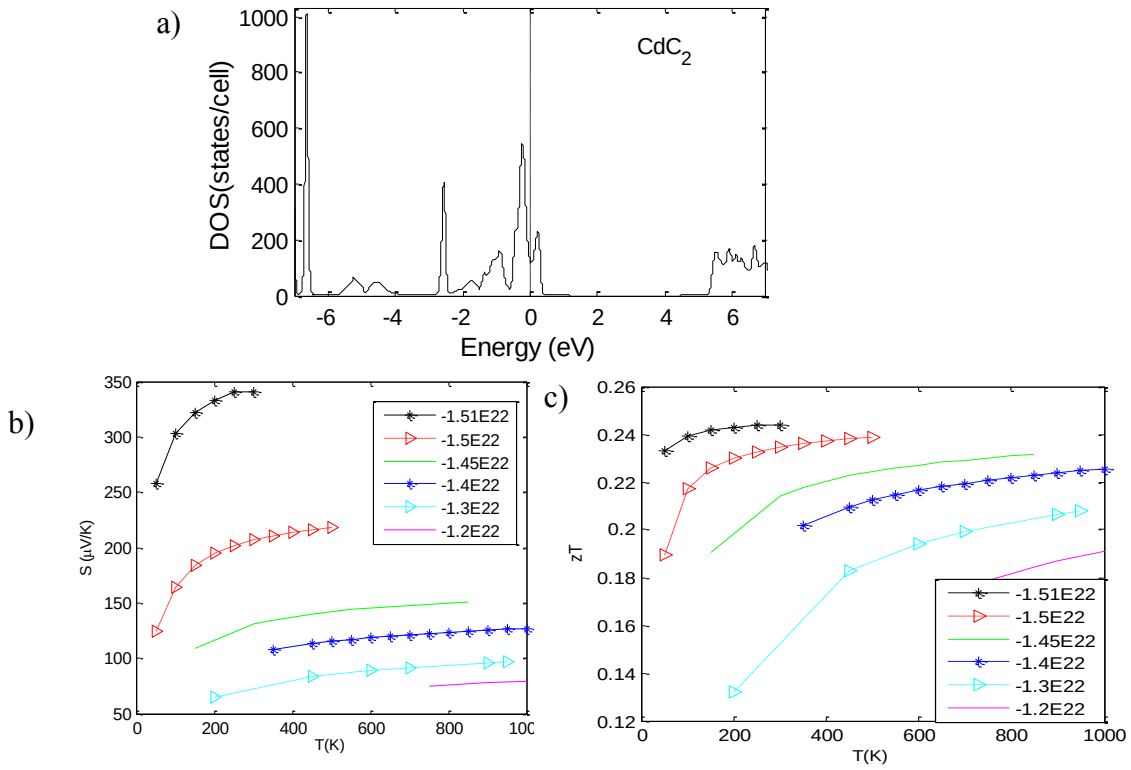

FIG. 2.46. CdC_2 DOS, S-T and zT plots. a) DOS, b) Seebeck coefficient and c) zT plots of CdC_2.

CHAPTER III

THE SPECIAL CASE OF $LaCoO_3$

Spin state transitions are usually attributed to a pressure variation, or triggered by an external E-field/magnetic perturbation (like - the behavior of a paramagnetic, often put to use in spin valves and spin flip techniques[38]) or are temperature driven. $LaCoO_3$ shows a similar spin state transition where magnetism shows up at about 100K. A procedure that enables the calculation of transport coefficients even in the presence of such phase transformations is outlined in this chapter. The transition temperature of $LaCoO_3$ is found to be 110 K which is 10% off the actual result[39] (~100K).

Two separate states of $LaCoO_3$ were initially prepared: an unadulterated state with lattice parameters obtained from ICSD, while the other state employs an overridden initial spin state (S=1). The geometries undergo full cell optimization with the aforementioned constraints with 8^3 (MHP) k-points in the irreducible wedge. A separate SCF calculation at an increased k (12^3) concentration helps retrieve dense ground state energies about the special points in the Brillouin zone, which are then supplied to BoltzTrap[40] as input. As expected, $LaCoO_3$ shows a Mott-behavior (*ref.* Fig.3.1, Fig3.2) unless one employs a L(S)DA+U. Similar effective (U-J) values were used for the High Spin (HS) state due to the absence of XPS data. Such an assumption could be one of the contributing factors to the ~10% error in the observation. Effective |U-J| parameters for Co are computed from the binding energies obtained from XPS data. "*Density functional study of CO on Rh(111)"* [41] is a formal discussion on the "how-to".

One notes from table 3.1 that the d electron occupancies are not whole numbers. DFT algorithms use integration techniques (over the charge density) that would obviously return a fractional component. Depending on the density of the k-mesh, the least significant digit (LSD) could be truncated. In general, fractional occupancies of less than unity are thanks to the hybridization of electrons. But anything over a 0.9 could be assumed to have minimal covalent character. The VASP input format of FERDO and FERWE (for spin polarized cases) requires that one fill the occupancies *corresponding to a* ***particular band*** by hand. There is, however no direct procedure to specify "d-states" for a particular atom exclusively. Establishing a relation between band energies and atom specific states requires a brute-force technique of scanning over each band to locate a specific d electron. Alternately, one could also use a small smear value (but

too small values < 1E-4 [Gaussian-smear] could render the program to malfunction[a] and terminate) and pinpoint the energy from an atom projected and band resolved partial-DOS plot[b].

TABLE 3.1. d-electron occupancies in LS, and spin polarized HS states. Table of partial occupancies for both HS and LS.HS state occupancies are "*put by hand*" assuming the d-electrons have no covalent contribution. In principle, the absence of the exact (like the 0.13 and the 0.14 in LS) occupancies is the main factor behind the 10 % deviation in the estimated Curie temperature. Other factors include: the use of effective (U-J) of the LS state in HS calculation, and also contribution from the subtleties that are natural in the DFT construct.

State	d_{xy}	d_{yz}	d_{zx}	$d_{(z2-x2)}$	$d_{(x2-y2)}$	E_g (eV)
LS (↑ ↓)	0.99	0.99	0.99	0.13	0.14	1.2
HS (↑)	1.0	1.0	1.0	1.0	1.0	0.8
HS (↓)	0	0	0	0	0	0.8

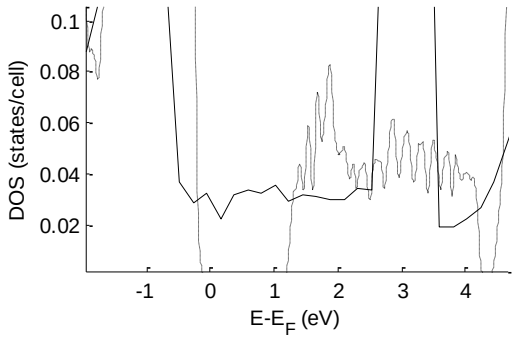

FIG. 3.1. Correlation effects in $LaCoO_3$. L(S)DA implementation (non-dotted line) of the LS state is plotted near the Fermi level as compared to the LDA (solid-line).

[a] The only reason to include a smear factor is to avoid singularities when one does a Fourier transform. $\mathcal{F}_x(e^{ik'\cdot x}) \rightarrow \delta(k-k')$ returns a diverging solution unless one uses an imaginary term (smearing).

[b] VASP parameter LORBIT=11 logs the site projected and band decomposed DOS.

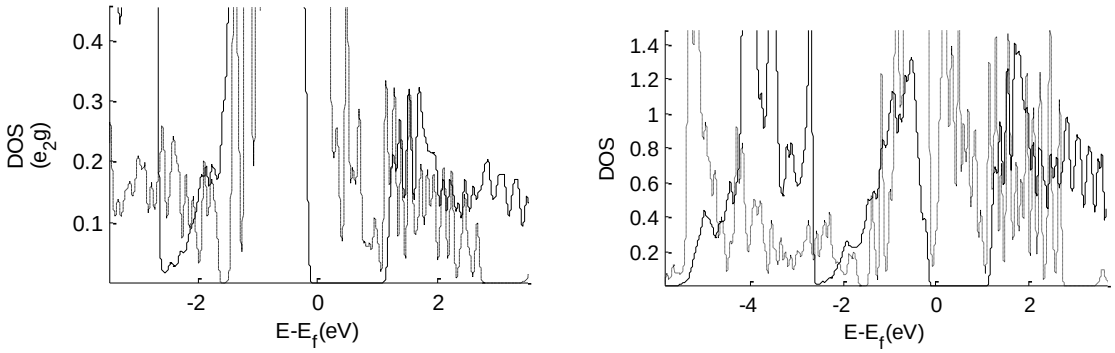

FIG. 3.2. t2g and eg contribution to correlation error. (***left***) Co eg level partial projection in the normal L(S)DA framework is compared to the splitting observed in the L(S)DA+U. (***right***) The t_2g levels are compared in the same principle. The state in the above calculation refers to the unaltered low spin state (S=0). U=5.9 and J=0.82.

It is a common practice in statistical theories and digital signal processing[42] to analyze similarity between two waveforms by computing the magnitude of cross-correlation. Mathematically, $X_{crr} = (S_1 \star S_2)(t) \stackrel{\text{def}}{=} \int_{-\infty}^{\infty} d\tau\, S_1(t) S_2(t+\tau)$ returns the continuous-variable time-dependent magnitude of cross-correlation between two waveforms, S_1 and S_2. Ignoring phase instabilities,

$$\mathrm{X_{crr}} = \max_{T}\{(S_1 \star S_2)(T_1)\} = max\left\{\sum_{\lambda=E_f-3}^{E_f+3} S_1(\mu, T_1) S_2(\mu+\lambda, T_1)\right\}.$$

Assuming a continuous transition between states (small transient) makes it a simple boundary value problem. But even within a state, as it is apparent from the samples that were studied in the earlier chapter, the Seebeck coefficient had a continuous change. We note that the cross-correlation function is bounded. Initially, a coarse dataset with 50 K spacing is used to cross-correlate data of the LS and HS systems. Presence of an extrema implies toggling the initial boundaries and reiterating the procedure until the LSD falls within the range of the tolerance. Since core electrons do not participate in the transport, a logical value of 3 eV was chosen so that the span of the sample set extends only to $E_f \pm 3$ eV. Using this procedure, Curie temperature of $LaCoO_3$ was found to be around 110 K (*fig.3.3*).

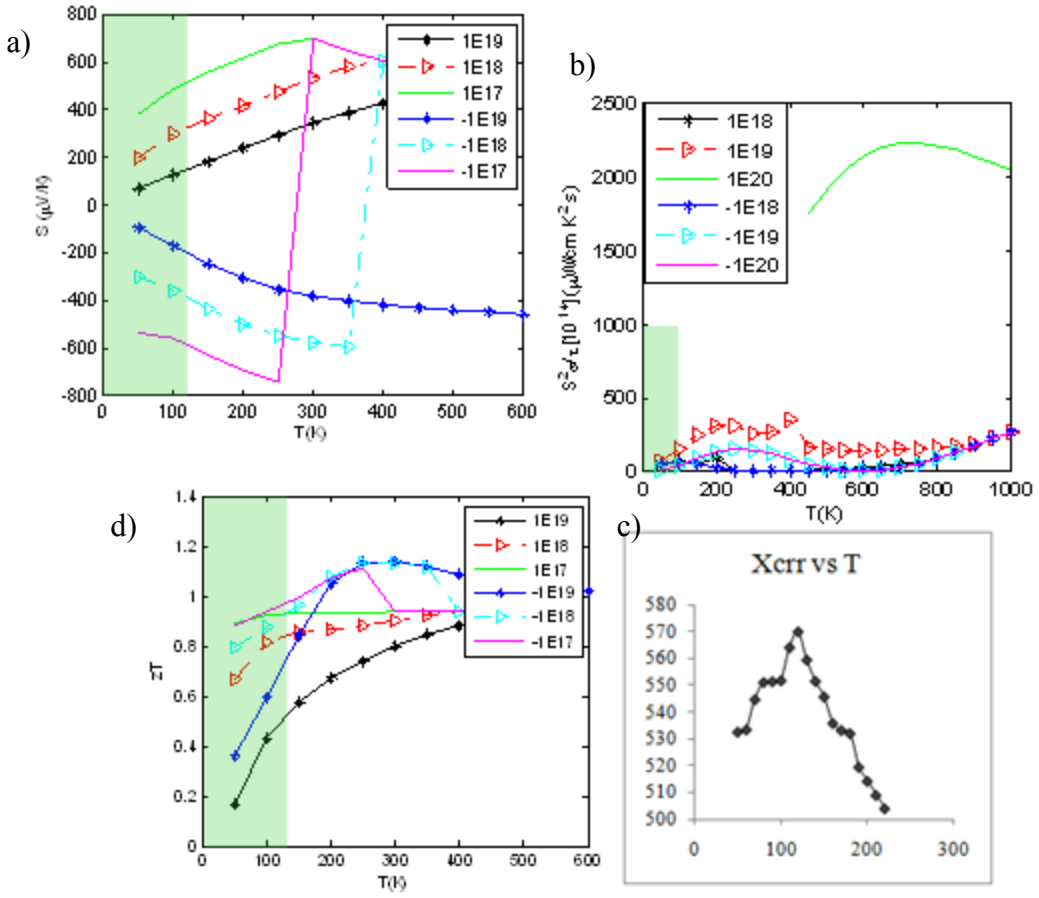

FIG. 3.3. TE performance obtained as a result of Seebeck cross-correlation treatment. a) S, b) power factor, c) cross-correlation and d) zT are plotted as functions of temperature. Region with a light green tinge corresponds to the LS state.

CHAPTER IV

CONCLUSION

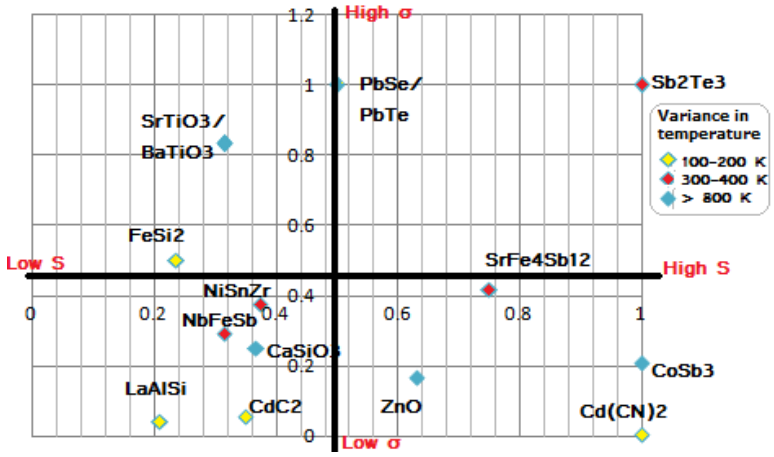

Element	T_{min}(K)	T_{max}(K)
NiSnZr	200	550
LaAlSi	50	200
NbFeSb	200	600
STO/BTO	200	1000
CaSiO3	50	1000
ZnO	50	200
FeSi2	50	250
$Cd(CN)_2$	50	100
CdC_2	200	1000
$CoSb_3$	600	1000
$SrFe_4Sb_{12}$	200	1000
Sb_2Te_3	200	600

FIG. 4.1. A grand-(Svsσ) plot categorically placing elements by the magnitude of S . The plot categorically places elements based on their normalized (max. value in the dataset) Seebeck coefficient and normalized σ parameters. The colored diamonds show the window width (with values [T_{min},T_{max}] tabulated in the adjacent table) of the consistency in the behavior of the thermoelectric parameters.

To summarize, this work discusses the role of *electronic contribution* to thermoelectric efficiency. Electronic contribution in the form of Seebeck coefficient is a crucial factor in estimating zT, since it scales as a squared factor, while the pure thermal counterparts (*like* k_l) scale linearly. One ought not to be deceived by the magnitude of zT alone. Wide-band gap semiconductors usually have a high Seebeck coefficient and show a capacitive behavior. And since Seebeck coefficient occurs as a squared factor in zT, the magnitude of zT does not give a true idea of the transport (ref. Fig.4.1). Prescription: Depending on the amperage requirements and impedance matching, one could migrate to the various regions on the chart (fig.4.1), choose an operating temperature range and pin-point a suitable material. Most materials have temperature tolerance bounds (fig.4.1) where in properties (as shown in fig.4.1) would remain invariant to temperature fluctuations (or are corrected by doping concentration).

Throughout this work, k_l is assumed to be zero and zT (as mentioned earlier) is defined as the maximum figure of merit at zero lattice thermal conductivity. It is a reasonable assumption

keeping in view the latest improvements in phonon engineering, Clathrate & filled Skutterudite systems, and mixed solutions that tend to decrease the lattice thermal conductivity without meddling much with the electronic structure. Quantitatively, k_l is a product of a rigorous molecular dynamics simulation exercise. Molecular dynamics incorporating statistical-mechanical procedures, or (Phonon) Boltzmann transport or response function formulations help determine the lattice thermal conductivity precisely. It all boils down to proper parameterization of force-fields for each system. Moreover, the correlated dependence of angle-angle, angle-bond and all possible parametric permutations of the cross-terms that contain most of the vibrational information, make the task far from being simple and general.

Two band models that were proposed in this work, offer a heuristic perspective to predict the essential thermoelectric parameters and most of all the models could be effectively expressed using toy-model basis functions (Chapter I and Chapter II). Advanced models and highly delocalized states that do not have steep band-edge could also be treated using toy models by introducing a random and scaled variation in the functional form of $E(k)$ (similar to Anderson's localization in disordered systems).

Experimental results have been fit to the calculated values to extract the complicated relaxation time. The limitations of rigid band approximation (PbSe: where the bandgap is sensitive to temperature) and constant-phase approximation (Ag_2Se: where there is a change of phase) have been highlighted, and a way to pre-conceive such occurrences are mentioned. Thermoelectric transport in the presence of a phase-change (*like* spin-transition) has also been analyzed and the Curie temperature was determined within a 10% accuracy.

REFERENCES

[1] C. Kittel, *Thermal physics* (Wiley, New York,, 1969).

[2] G. S. Nolas, D. T. Morelli, and T. M. Tritt, Annual Review of Materials Science 29, 89 (1999).

[3] R. G. Parr, Annual Review of Physical Chemistry 34, 631 (1983).

[4] E. H. Lieb and B. Simon, Physical Review Letters 31, 681 (1973).

[5] D. Jena, A. C. Gossard, and U. K. Mishra, Applied Physics Letters 76, 1707 (2000).

[6] A. Szabo and N. S. Ostlund, *Modern quantum chemistry: introduction to advanced electronic structure theory* (Dover Publications, Mineola, N.Y., 1996).

[7] M. P. Marder, *Condensed matter physics* (John Wiley, New York, 2000).

[8] M. Lundstrom, *Fundamentals of carrier transport* (Cambridge University Press, Cambridge, 2000).

[9] P. A. M. Dirac, Proceedings of the Royal Society of London Series A-Containing Papers of a Mathematical and Physical Character 112, 661 (1926).

[10] J. Androulakis, C. H. Lin, H. J. Kong, C. Uher, C. Wu, et al., Journal of the American Chemical Society 129, 9780 (2007).

[11] Y. Gelbstein, Z. Dashevsky, and M. P. Dariel, Physica B-Condensed Matter 363, 196 (2005).

[12] P. F. P. Poudeu, J. D'Angelo, H. J. Kong, A. Downey, J. L. Short, et al., Journal of the American Chemical Society 128, 14347 (2006).

[13] Y. Zhang, X. Z. Ke, C. F. Chen, J. Yang, and P. R. C. Kent, Physical Review B 80, 024304 (2009).

[14] C. M. Fang, R. A. de Groot, and G. A. Wiegers, Journal of Physics and Chemistry of Solids 63, 457 (2002).

[15] N. Piccioli, J. M. Besson, and Balkansk.M, Journal of Physics and Chemistry of Solids 35, 971 (1974).

[16] A. Lipovskii, E. Kolobkova, V. Petrikov, I. Kang, A. Olkhovets, et al., Applied Physics Letters 71, 3406 (1997).

[17] T. Kyratsi, J. S. Dyck, W. Chen, D. Chung, C. Uher, et al., Journal of Applied Physics 92, 965 (2002).

[18] C. M. Bhandari and D. M. Rowe, *Thermal conduction in semiconductors* (Wiley, New York, 1988).

[19] M. Ferhat and J. Nagao, Journal of Applied Physics 88, 813 (2000).

[20] M. Schluter, G. Martinez, and M. L. Cohen, Physical Review B 12, 650 (1975).

[21] H. J. Monkhorst and J. D. Pack, Physical Review B 13, 5188 (1976).

[22] M. C. S. Kumar and B. Pradeep, Semiconductor Science and Technology 17, 261 (2002).

[23] D. Y. Chung, T. Hogan, P. Brazis, M. Rocci-Lane, C. Kannewurf, et al., Science 287, 1024 (2000).

[24] G. F. Wang and T. Cagin, Physical Review B 76 (2007).

[25] J. Kubler, A. R. Williams, and C. B. Sommers, Physical Review B 28, 1745 (1983).

[26] J. Pierre, R. Skolozdra, J. Tobola, S.Kaprzyk, C. Hordequin, et al., Journal of Alloys and Compounds 262, 101 (1997).

[27] H. Hohl, A. P. Ramirez, C. Goldmann, G. Ernst, B. Wölfing, et al., Journal of Physics-Condensed Matter 11, 1697 (1999).

[28] T. Sekimoto, K. Kurosaki, H. Muta, and S. Yamanaka, Journal of Alloys and Compounds 407, 326 (2006).

[29] B. R. K. Nanda and I. Dasgupta, Journal of Physics-Condensed Matter 15, 7307 (2003).

[30] F. G. Aliev, N. B. Brandt, V. V. Moshchalkov, V. V. Kozyrkov, R. V. Skolozdra, et al., Zeitschrift Fur Physik B-Condensed Matter 75, 167 (1989).

[31] Q. Shen, L. Chen, T. Goto, T. Hirai, J. Yang, et al., Applied Physics Letters 79, 4165 (2001).

[32] N. W. Ashcroft and N. D. Mermin, *Solid state physics* (Holt, New York,, 1976).

[33] S. Ohta, T. Nomura, H. Ohta, and K. Koumoto, Journal of Applied Physics 97 (2005).

[34] H. Ohta, Materials Today 10, 44 (2007).

[35] V. N. Antonov, O. Jepsen, W. Henrion, M. Rebien, P. Staub, et al., Physical Review B 57, 8934 (1998).

[36] N. E. Christensen, Physical Review B 42, 7148 (1990).

[37] J. D. Corbett, Chemical Reviews 85, 383 (1985).

[38] S. Datta and B. Das, Applied Physics Letters 56, 665 (1990).

[39] H. Hsu, K. Umemoto, M. Cococcioni, R. Wentzcovitch, Physical Review B 79 (2009).

[40] G. K. H. Madsen and D. J. Singh, Computer Physics Communications 175, 67 (2006).

[41] L. Kohler and G. Kresse, Physical Review B 70 (2004).

[42] J. G. Proakis and D. G. Manolakis, Digital signal processing (Pearson Prentice Hall, Upper Saddle River, N.J., 2007).

VITA

Shiv Akarsh Meka received his Bachelors of Technology in electronics and communication from VIT, India in 2007. His research interests are centered in quantum transport and strongly correlated systems. In 2008, he interned at Ames Research Center. He is currently a member of the IEEE and also a reviewer of Journal of Nanotechnology. He can be reached at:

Shiv Akarsh Meka,
3003 TAMU,
College Station
TX 77843
shivakarsh@gmail.com